IMAGING OF *CAENORHABDITIS ELEGANS* WITH NEAR INFRARED SPECTRALLY ENCODED CONFOCAL MICROSCOPY

SADAF RASHTCHIAN

A THESIS SUBMITTED TO THE
FACULTY OF GRADUATE STUDIES
IN PARTIAL FULFILLMENT OF THE
REQUIREMENTS FOR THE DEGREE OF
MASTER OF APPLIED SCIENCE

GRADUATE PROGRAM IN MECHANICAL ENGINEERING
YORK UNIVERSITY
TORONTO, ONTARIO

June 2021

Abstract

Caenorhabditis elegans (*C. elegans*) is an optically transparent nematode that shares many gene orthologs and homologs with humans. *C. elegans* is widely used in large populations for genetic studies relevant to human biology and disease. Success of such studies frequently relies on the ability to image *C. elegans* structure at high-resolution and high-speed. To date, fluorescent confocal, light sheet, two photon, brightfield and differential contrast microscopy techniques have been widely used to investigate human diseases from understanding disease pathology to screening for chemicals toxicity and therapeutic effects. However, these techniques cannot provide all the characteristics needed for high-throughput imaging of *C. elegans*. Fluorescent techniques need labeling, which can increase the sample preparation time, and, in some case, it may cause phototoxicity; on the other hand, non-fluorescent techniques lack the contrast needed to resolve internal organs of the nematode. Therefore, this thesis is aimed at determining the feasibility and sustainability of a high-speed variant of reflectance confocal microscopy, known as spectrally encoded confocal microscopy (SECM), for label free imaging of *C. elegans*.

The developed system utilizes near-infrared illumination in conjunction with refractive and diffractive optics to instantaneously image a confocal image line at a speed of up to 147 kHz with lateral and axial resolutions of 2 μm and 10 μm, respectively. Our imaging results from wild-type *C. elegans* and four mutant strains (MT2124, MT1082, CB61, and CB648) demonstrate the ability of SECM in revealing the overall geometry, key internal organs, and mutation-induced structural variations at an unprecedented imaging speed.

Dedication

To my mother and father.

Acknowledgments

I would like to express my sincere gratitude to Prof. Tabatabaei for his unconditional support and guidance all throughout my research.

Table of Contents

List of Figures

List of Tables

Chapter 1
Introduction

This chapter aims to highlight the importance of model organism *C. elegans* in biology and medicine, provide an overview on the popular fluorescent and non-fluorescent imaging techniques commonly used to screen and investigate the model organism, and highlight the need/gap in high-speed imaging of *C. elegans*. Toward the end of the Chapter, I discuss how the rapid confocal microscope developed in this thesis can fill the current technological gap.

1.1. What is model organism?

Model organism refers to any non-human organism which is used to investigate a biological process or system [1]. They are valuable since investigations on them can be generalized to study other animals or even humans. Model organisms are widely used in human disease studies, drug delivery, behavioral screening, and genetic investigations [2]. For instance, drug delivery trials often fail due to ineffective drug distribution and absorption or chemical toxicity. Investigating the whole animal in a cost-effective and fast manner (like monitoring the actual behavioral response of the model) can reduce these failures [3]. The nematode worm *Caenorhabditis elegans*, zebrafish *Danio rerio*, and the fruit fly *Drosophila melanogaster* are three of the thirteen species listed by the U.S. National Institute of Health (NIH), showing

promising characteristics which can bridge cell-based investigations to whole-animal studies [1]. The key advantage of model organisms is that, unlike mammalians, there are no ethical considerations involved in performing biological experiments on them, which enables us to investigate a large population of them in drug discovery and disease studies [2]. Ability to study large populations is key for making statistically meaningful conclusions on the efficacy of drugs under investigation.

1.2. *C. elegans* as a model organism

C. elegans is a versatile model organism for studying a broad spectrum of human diseases. The life cycle of *C. elegans* in 25°C is approximately three days. Like other nematodes, it starts at the embryonic stage, followed by four larval stages (L1-L4) and adulthood (Figure 1(A)) [4]. *C. elegans* is easy to culture in an unsterile environment, and each nematode is capable of producing 300-350 progenies by self-fertilization in the adult stage [5], which makes it a cost-effective model organism for drug discovery and disease studies [6].

C. elegans has a length of ~1mm and a diameter of ~50 μm in young adult stages. Despite the small size, *C. elegans* emerges to have many organs found in complex organism, like digestive system, musculature and reproductive system [7]. The small size, along with the optically transparent nature of the worm, enable investigating molecular and cellular features using different microscopy techniques [4]. Most importantly, *C. elegans* has a fully sequenced genome and shares many gene orthologs and homologs with humans (many related to human diseases). Different human disorders such as neurodegenerative diseases, diabetes, and cancer have been modeled using *C. elegans* to understand disease pathology further and provide a drug screening model [8].

C. elegans neuronal, cellular, and behavioral phenotypes can offer reliable readouts of genetic mutation and drug screening. For instance, genetic mutations in lung cancer associated genes were found to cause a deficiency in *C. elegans* vulva development or to induce a multi-vulva (Muv) phenotype [4]. Other mutations of *C. elegans* which alter egg laying behavior in the nematode can be studied in drug screening in glucose assay investigations [6].

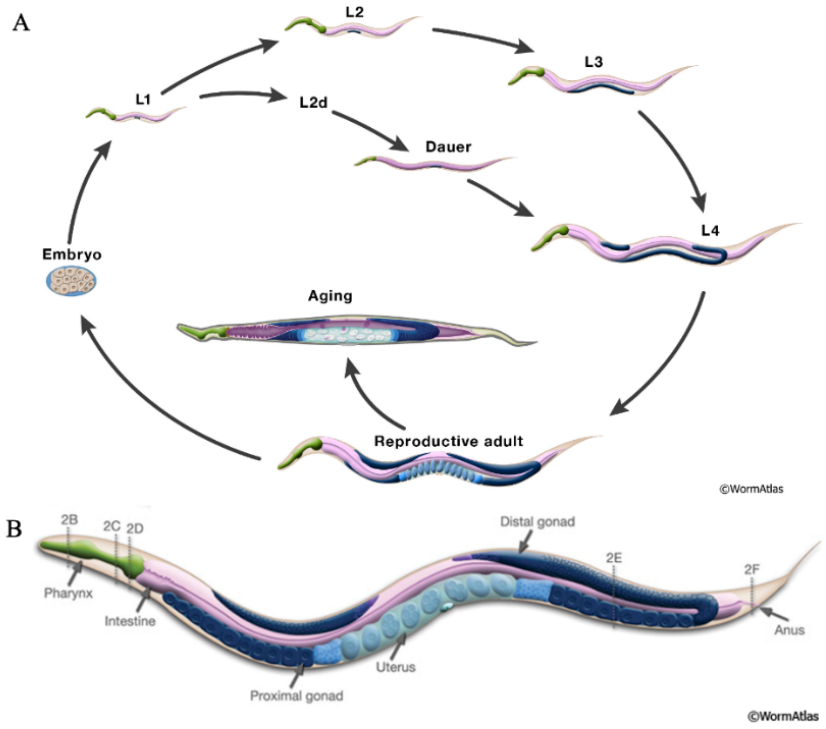

Fig.1.1 A) life cycle of *C. elegans*. B) *C. elegans* anatomy in adult stage [9].

Behavioral studies of *C. elegans* have also proved to be beneficial for drug screening for human diseases. For example, phenotypic screening of behaviors like pharyngeal pumping rate as a measure for food intake has been utilized for drug screening due to the ease of monitoring the synchronous motion of the grinder movements [8]. Another example is the Parkinson's disease worms with alpha-syn mutation which showed a significant decrease in their pharyngeal pumping rate but the condition was alleviated using anti-Parkinsonian compounds [4, 8, 10, 11]. The success of the abovementioned biological investigations relies on the ability to screen large

populations of worms to reach statistically meaningful conclusions. Given the small size and optical transparency of *C. elegans*, imaging the worms at high resolution is necessary for interrogation and screening of cells and organs of interest (e.g., neurons, eggs, vulva, isthmus, corpus, and intestine). Therefore, success of Biological studies relies on development of high-throughput imaging technologies that can rapidly image thousands of *C. elegans* at high resolution. In general, microscopic technologies for imaging *C. elegans* can be divided into two groups: fluorescent and non-fluorescent microscopy techniques. Sections below offer a brief overview of these imaging technologies and discuss their advantages and limitations for high-throughput screening of large populations of *C. elegans.*

1.2.1. Fluorescent methods

Fluorescent microscopy techniques are normally the preferred interrogation method for studying *C. elegan*s mutagenesis. The source of image contrast in these techniques is normally fluorescence of Green Fluorescent Protein (GFP). GFP is widely used as a molecular tool to assess protein expression and localization. To date, confocal fluorescent microscopy (CM), light sheet fluorescent microscopy (LSFM), selective plane illumination microscopy (SPIM), and two-photon microscopy have been exploited to probe *C. elegans* cellular and neuronal activities. The transparency of *C. elegans* allows proteins and neuron expressions to be imaged [12]; optical sectioning and 3D imaging are other key advantages of most fluorescent techniques.

In general, confocal microscopy uses reflected light or fluorescent light same as conventional light microscopy, however, in CM the out of focus light is excluded from reaching the detector by use of a spatial filter/pinhole. Thus, confocal microscopy results in better contrast and reveals fine details in the image [13]. Figure 1.2 shows a simplified schematic of a confocal microscope.

In this technique, based on the goal of study, specimens can be tagged with different fluorophores and subsequently imaged [14].

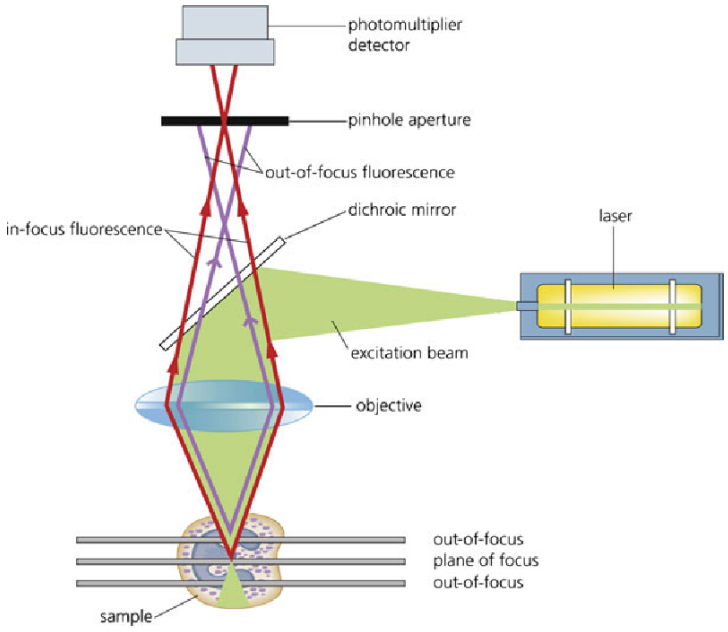

Fig. 1.2. Schematic of a confocal microscope [15]. Pinholes in the illumination and detection path reject the out of focus light.

Fluorescent CM is perhaps the most frequently used fluorescent technique for imaging live *C. elegans* [16]. For instance, Parkinson's disease (PD) can cause loss of dopaminergic neurons (DNs) in the substantia nigra and accumulation of α-synuclein protein, which both can be studied in *C. elegans* neuronal system with Fluorescent CM. Quantification of amount of fluorescence is also achievable by CM. For example, in PD research, the intensity of green fluorescent proteins (GFP) of dopamine transport gene (dat-1) is measured to assess DNs survival [12]. Figure 1.3(A) shows GFP expressions in DNs of transgenic *C. elegans*. Images of α-syn accumulation over time in the presence and absence of Chondruc Crispus are shown in panel B. Fluorescent CM, however, is only useful for imaging cells or organelles that can be tagged with fluorophores [12]. Photodamage and slow imaging speed are other key limitations

of this method. Recently, LSFM and SPIM have been proposed to overcome the slow speed and phototoxicity issue of CM [17, 18].

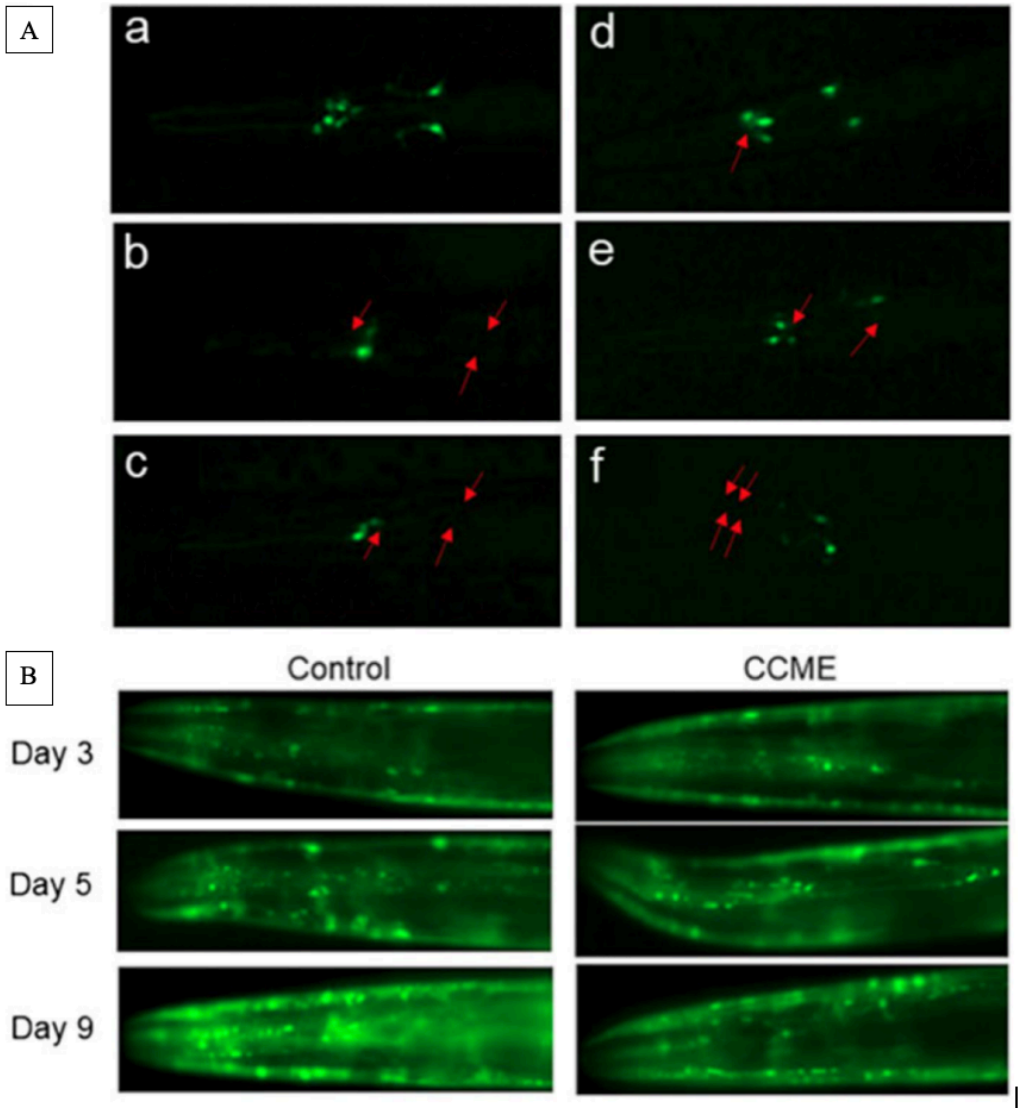

Fig.1.3. A) GFP expression in DNs of transgenic *C. elegans* strain UA57. (a) image for the intact DNs, (b-f) DNs loss under the exposure to 6-OHDA, with the red arrows indicating the degenerated/ missing neurons. Images of α-syn accumulation over time in the presence and absence of Chondruc crispus B) The methanolic extract of Chondruc crispus rescues 6-OHDA induced DNs degeneration and reduces α-syn accumulation in NL5901 [12].

In LSFM (also termed as SPIM), two perpendicular objectives are used to separate the illumination and fluorescent detection channels. These two objectives are normally aligned such

that the generated thin light sheet only illuminates the focal plane of the detection objective. The sample is usually mounted vertically in a motorized chamber that incrementally moves the sample through the focus of the system (Figure 1.4). In this configuration, high resolution fluorescent images of sample cross sections can be acquired at once with minimal photodamage. However, the size and short working distance of this technique pose practical limitations for imaging larger samples [19]. In addition, the need for mechanical scanning and rotation of sample through the focus of the system make this imaging technology unsuitable for high throughput imaging applications of populations of model organisms.

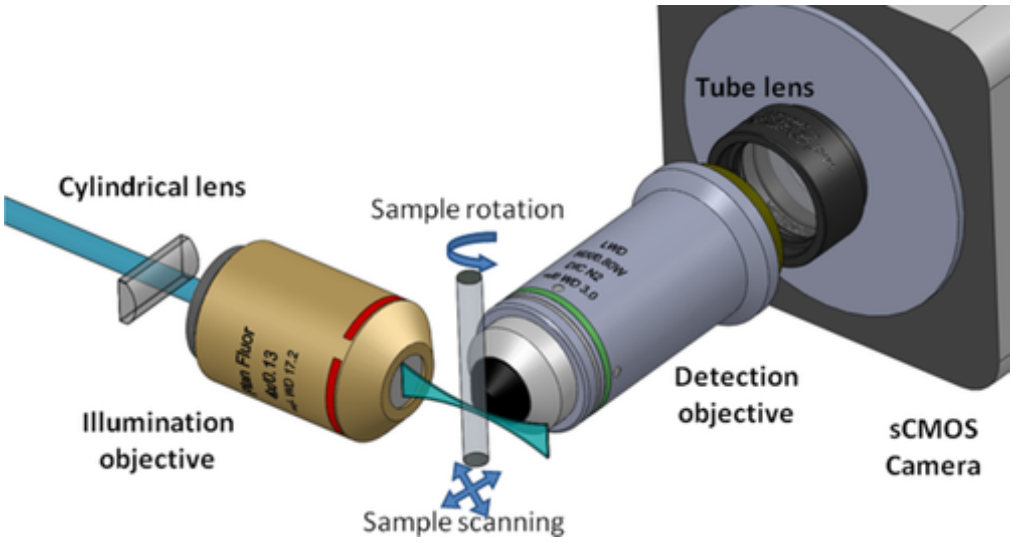

Fig. 1.4. Schematic diagram of the light-sheet fluorescence microscopy concept [20].

Figure 1.5(A,B) depicts images of *C. elegans* oocyte and embryo taken with a compact LSFM system[19]. Figure 1.5C depicts a 3D reconstruction of *C. elegans* with proteins tagged with YTF, imaged by the LEAD (line excitation array detection) system [17].

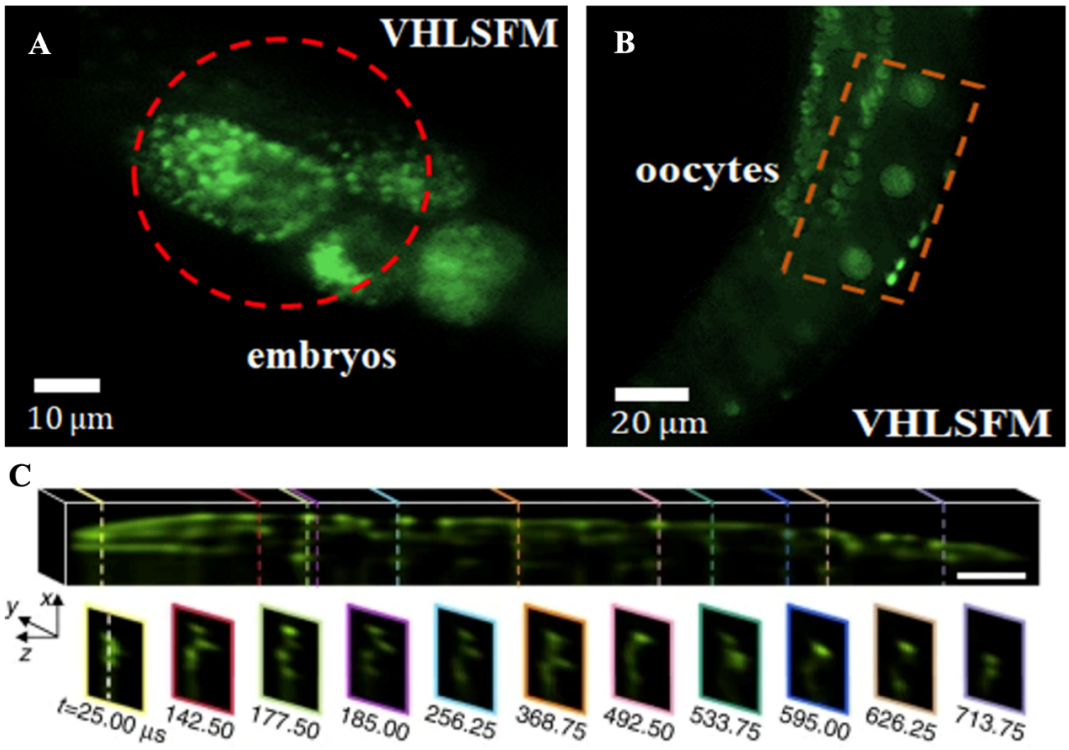

Fig. 1.5. A) Volume holographic optical element for light sheet fluorescence microscopy[19], LEAD fluorescence microscopy at 0.8 million frames per second [17].

Two-photon excitation (TPE) microscopy is another alternative for 3-dimensional imaging of cells. TPE can reduce phototoxicity with respect to conventional single-photon confocal microscopy. Unlike Fluorescent CM which provides a single-photon excitation, the laser in TPE excites by using near simultaneous absorption of two long wavelength (~800 nm) photons. As depicted in Figure 1.6, TPE results in a much smaller point spread function as absorption of two photons is only likely in the focus of the system. Since two-photon excitation is only achievable near the focal plane, there is minimal damage to the tissues above and below the plane and there is also no out of focus light to make the images blurry [21, 22].

Two-photon fluorescent microscopy has also been implemented to obtain information on different cell types of *C. elegans*. This technique can reduce the phototoxicity and

photobleaching caused by fluorescent CM [22]. However, TPE microscopy is also prone to slow imaging speed and also requires the use of expensive femtosecond lasers.

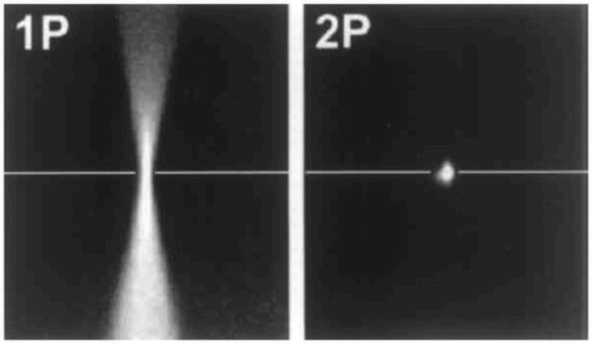

Fig.1.6. Distribution of fluorescein fluorescence in the *x*-*z* plane during A) single-photon (1P) excitation by focused 488-nm laser light and (B) during two-photon (2P) excitation using femtosecond pulses of 850-nm light [21].

The common denominator of above fluorescent microscopy techniques is the reliance on fluorescent labeling that not only increases the sample preparation time and complexity, but also can interfere with cellular processes [23]. Moreover, since fluorescent-based techniques image GPF expression they are not suitable for physiological and behavioral phenotype screening due to absence of fluorescence expression in entire *C. elegans* body. For such studies, non-fluorescent microscopy techniques are used.

1.2.2. Non-fluorescent microscopy techniques

Conventional brightfield microscopy has a wide range of applications from basic biology to investigating cell structures biology in microbiology and cell biology [24]. This technique offers limited contrast and lacks optical sectioning ability, resulting in low resolution due to reflections from sample structures outside the focus. Figure 1.7 depicts an image of the nematode taken with brightfield microscopy. As can be seen, the native poor contrast of brightfield microscopy prevents reliable visualization of the internal organs of the nematode. In addition, lack of optical

sectioning results in superposition of organs within the depth of field of the objective, making it impossible to resolve the internal structures of *C. elegans* within the cross sections.

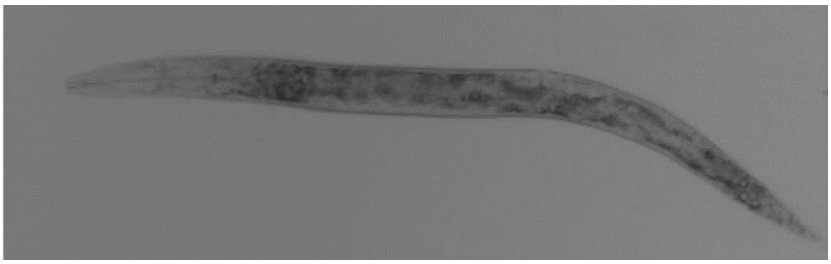

Fig. 1.7. Brightfield image of *C. elegans* [25].

In comparison to brightfield microscopy, differential interference contrast microscopy offers high contrast images, making it a popular technique to image *C. elegans* of different stages. Figure 1.8 depicts a schematic of a DIC microscope. In DIC, the linearly polarized light splits into two components via a prism; then, the split rays interact with the sample and finally recombines by another prism to enter the objective lens to form interferometric images of the sample on the detector [16].

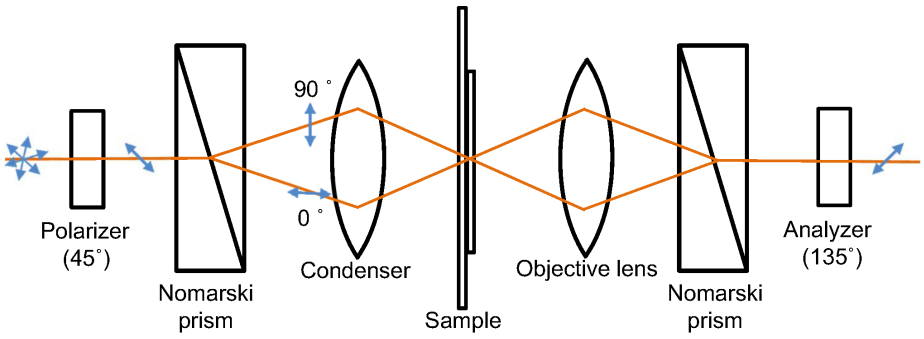

Fig 1.8. Schematic of a DIC setup [26].

In such system, the varying thickness and refractive indices of specimen result in an optical path length gradient, which creates high contrast pseudo-3D relief shading images of a specimen [16]. Figure 1.9 A shows a DIC image of adult *C. elegans*; only shadows of the organs like pharynx and oocytes can be seen in this panel. DIC image of the pharyngeal region of the worm

is depicted in panel B. As shown in the figure, despite the high resolution of the image, different regions such as Procorpus, Metacorpus, and Isthmus are not well-resolved due to lack of contrast. Key limitation of DIC, however, is that its image brightness is less than that of brightfield microscopy, which makes sample illumination challenging at high magnifications. Lack of optical sectioning and 3D imaging in DIC is another key limitation of the technique, leading to superposed and blurry DIC micrographs of *C. elegans* internal organs [23].

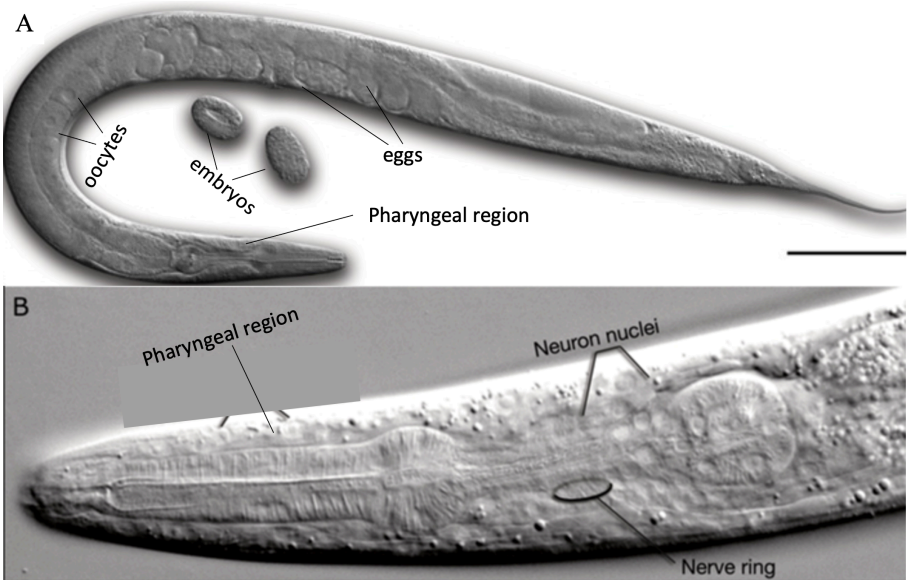

Fig. 1.9. A) DIC micrograph of gravid *C. elegans* and its embryos [9], B) mages of the head of a young adult animal at three planes, viewed from the left side [27],

Above brief review of non-fluorescent microscopy techniques suggests that there is currently no technology that offer high-resolution/confocal imaging of *C. elegans* internal structures at high speed. Such structural images of populations of worms are essential to the success of physiological and behavioral phenotype screening studies of *C. elegans*.

1.3. Objective of thesis

C. elegans has emerged as one of the most important model organisms since 1998 when the genome map of the nematode was completed. The literature review on microscopy technologies for imaging *C. elegans* highlights the need for high-speed imaging platforms that offer high-resolution images to enable high-throughput physiological and behavioral phenotype screening based on worms' intrinsic contrast and geometry. Despite the need, existing microscopy methods cannot provide a combination of fast, label-free, and high-resolution systems for imaging the nematode. For this matter, this thesis reports on developing a high-speed variant of reflectance confocal microscopy, named Spectrally Encoded Confocal Microscopy (SECM). SECM can be used for high-speed confocal imaging of *C. elegans* and this research aims to identify the advantages and limitations of this technology.

The first chapter of the thesis focuses on the importance of *C. elegans* and current popular methods for imaging the nematode.

Chapter two presents the theoretical background of the SECM and a review of applications of the system.

Chapter three describes the optical design and assembly of the microscopy system. Moreover, in this chapter, an overview of the standard phantom tests and sample preparation of *C. elegans* are described.

Chapter four discusses the results of the optical performance measurements and establishes the feasibility of imaging wild-type and mutant *C. elegans* with SECM.

Chapter five brings together the conclusions of the research presented in this thesis and recommends future directions.

Chapter 2

Spectrally encoded confocal microscopy

This chapter offers a brief review on background and theory of Spectrally-Encoded Confocal Microscopy (SECM). A literature review of current technological achievements in the field of SECM is also offered.

2.1. Background

Confocal microscopy is a technique in which out of focus light from the sample is rejected through spatial filters (aka. pinhole apertures) in the illumination and detection paths. By doing so, confocal microscopy can produce thin image slices of sample (aka. optical sectioning), enabling resolution of detailed internal structures of sample. This optical sectioning is relatively non-invasive, so it allows us to observe living samples with great clarity [28]. For many years, biologist used confocal microscopy to observe microstructure of specimens with high resolution [29]. However, as the confocal aperture blocks most of light reflecting from the tissue, a powerful light source like laser is in demand. Without laser, it will take a considerable time to

record an image. Another problem in this technique, is single point illumination and detection scheme, which means the system is only able to measure one point of the image at a time. Therefore, to record an image it should sequentially image single points within the specimen. Same time-consuming process needs to be repeated at other depths of sample to produce confocal volumetric datasets. To alleviate the speed issue, laser scanning confocal microscopes have been developed [29], in which an automated system is added to the microscope to mechanically scan the laser beam across the sample. However, the mechanical scanning approach increases the size, complexity and cost of the system and also makes the system unsuitable for studying fast biological processes over time. In order to overcome some of the limitations of confocal microscopy, a fiber optic-based configuration of confocal microscopy, named spectrally encoded confocal microscopy (SECM), has recently been introduced [28].

2.2. Principles of SECM

SECM is a high-speed and fiber-optic-based variant of reflectance confocal microscopy. In SECM, a diffraction grating-objective lens pair is used to focus/encode different wavelengths of a broadband laser light on a transverse confocal line inside the sample while reflections from the confocal line are continuously recorded with a spectrometer [30]. Enhancement of imaging speed in SECM is due to the ability to instantaneously image a confocal line. Figure 2.1 depicts the schematic of a spectrally encoded imaging instrument.

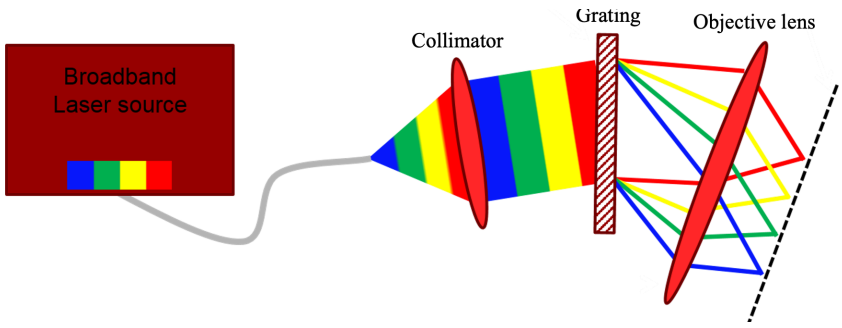

Figure 2.1. Spectrally encoded imaging.

The core of the optical fiber (~8μm for single-mode SMF28 fiber) is a flexible conduit for light which in SECM serves as the confocal pinhole aperture to reject the out of focus light and thus offers optical sectioning of the sample [31]. In SECM, a broadband laser light illuminates the optical fiber, which is then collimated on a transmission diffraction grating. The grating diffracts each wavelength of the broadband light source at a unique angle, and then each wavelength is focused by a high numerical aperture (NA) objective on a transverse confocal line inside the specimen [30, 31]. Chromatic aberration of the objective lens is also a factor that enables encoding the information [31]. The light reflected by the sample is then transmitted back in the same optical path through the optical fiber, which rejects the out of focus light from the sample. Subsequently, a spectrometer analyzes the reflected light from sample, revealing the amount of reflection from each point of the imaged confocal line at once [30]. To form two dimensional images, the confocal line can be laterally translated via a scanning mirror, or alternatively, the sample can be translated through the stationary confocal line [31]. Section below depicts theoretical formulation of SECM which we used for the design and development of our system.

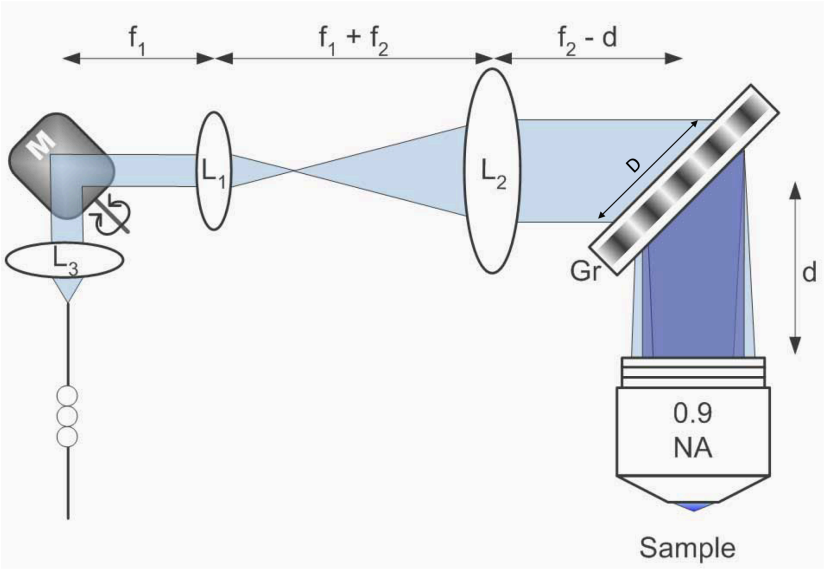

Fig. 2.2. Schematic of SECM system. L: lens, M: galvanometer mirror, Gr: diffraction grating, f: focal length [32] .

The most important performance metrics of an SECM system are axial and lateral resolutions and field of view (FOV). The lateral resolution (δx) of the spectrally encoded confocal microscope is a multifactorial metric, governed by the spot size produced by the objective lens, resolving power of the diffraction grating, and spectral resolution of the spectrometer [31]. Based on the Rayleigh criterion for monochromatic confocal microscopy, lateral resolution is given by [31]:

$$\delta x = \frac{0.56\lambda}{NA} \tag{2.1}$$

Where λ and NA are center wavelength of the broadband laser light, and numerical aperture of the objective lens, respectively. The numerical aperture of a lens defined as:

$$NA = n \sin \alpha \tag{2.2}$$

Where n is the refractive index of the medium (i.e, n=1 for our case), and α is the half angle of the cone of light which can be collected by the objective lens. NA is a number without units, and it is important since it affects both lateral and axial resolution in confocal microscopy.

Optical sectioning ability of a confocal microscopy system, which is referred to as axial resolution is also dependent on the NA and it is given by [31]:

$$\delta z = \frac{0.9n\lambda}{(NA)^2} \tag{2.3}$$

In the imaging arm the spectral resolving power of the grating (i.e., ability to discern between different wavelengths) is calculated by [31, 33]:

$$\delta\lambda = \frac{\lambda\Lambda}{mD} \tag{2.4}$$

Where λ is the center wavelength, D is the beam diameter along the grating, m is order of diffraction, and Λ is the grating period. Therefore, the resolving power of a diffraction grating in an SECM system is given by [31, 33]:

$$R = \frac{\Delta\lambda}{\delta\lambda} \tag{2.5}$$

Where $\Delta\lambda$ is the full width at half maximum (FWHM) bandwidth of the laser. In an SECM system where spatial sampling of the objective lens in matched with the spectral resolution of the grating the following relationship holds [31]:

$$\frac{FOV}{\delta x} = \frac{\Delta\lambda}{\delta\lambda} \tag{2.6}$$

While above relationship determines the maximum achievable FOV, often the left-hand side of the equation is intentionally kept smaller than the right-hand side to oversample the spectrally encoded line. Equation 2.6 can also be used to calculate the number of resolvable points in wavelength dispersed axis. That is, the length of line of focus can be determined by [31]:

$$FOV = 2ftan\frac{\Delta\theta}{2} \quad 2.7$$

Where f is the effective focal length of the objective lens, and $\Delta\theta$ is the deviation between diffracted angles of the wavelength extremities. $\Delta\theta$ can be found by [31, 33]:

$$\Delta\theta = \frac{m \times \Delta\lambda}{\theta_l \times \Lambda} \quad 2.8$$

In Equation 2.8 θ_l is the Littrow's angle. At this incident angle the first order grating efficiency is the highest. Another design parameter of an SECM system is proper sampling of wavelengths by the spectrometer. That is, the spectral resolution of the spectrometer must be at least twice that of the diffraction grating to allow for Nyquist sampling.

2.3. SECM in biology

Previously, reflectance confocal microscopy (RCM) was used to visualize cellular features of human tissue, however the bulky nature of RCM limited its translation to Medicine in form of probes and endoscopes [34]. SECM, on the other hand, utilizes the concept of wavelength division multiplexing to encode one dimension of the confocal image by use of a diffraction grating. This configuration eliminates the need for mechanical beam scanning inside SECM devices and thus promote high speed RCM imaging with miniaturized SECM probes and endoscopes. These appealing features of SECM have made the technology a good candidate for *in-vivo* studies. Sections below offer a brief review of clinical applications of SECM to date.

2.3.1. Spectrally encoded flow cytometry

Flow cytometry is a technique used for quantifying the population of cells or particles. Conventionally fluorescent labels have been used to provide information on cell size, shape,

and blood samples' properties [35]. Although *ex-vivo* analysis provides quantitative information on the cells, it cannot provide real-time data and requires blood extraction from patients [36]. By taking advantage of the unidirectional blood flow in the vessels, a SECM technique known as spectrally encoded flow cytometry (SEFC) has been proposed for high-resolution *in-vivo* imaging and quantification of blood cells without any mechanical scanning. Acquiring images of the transverse spectrally encoded line within the vessels results in a two-dimensional image in which one axis represents the confocal line, and the other axis represents the time (Figure 2.3) [35, 36]. Using this approach, SEFC was used to measure the red blood cell diameter, and the acquired data was found to be highly correlated with the *ex-vivo* measurements. Also, the functional area occupied by red blood cells (RBC) was shown to offer an accurate estimate of the hematocrit in the patients (Figure 2.4) [36].

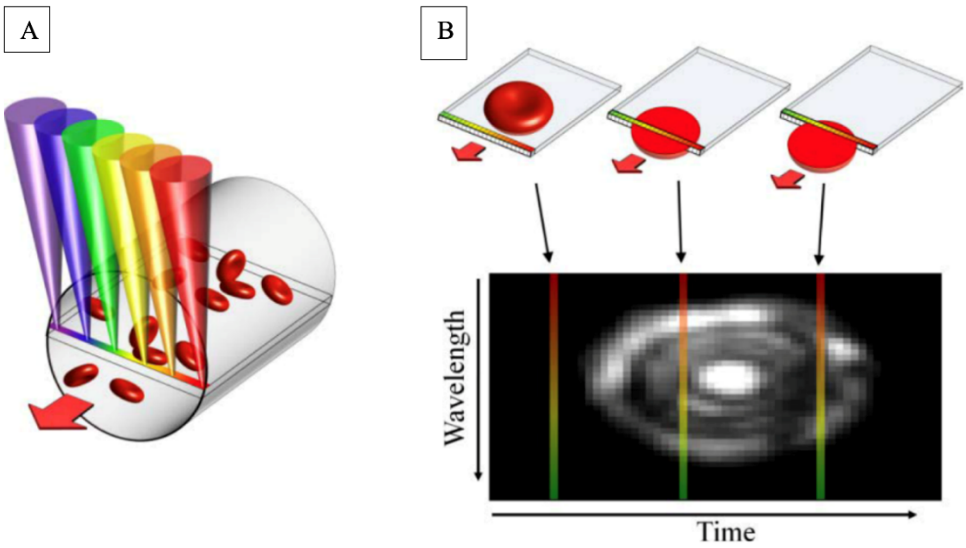

Fig. 2.3. Image acquisition in SEFC. A) A single line within a blood vessel is imaged with multiple colors of light that encode lateral positions. B) A single cell crossing the spectral line produces a two-dimensional image with one axis encoded by wavelength and the other by time [36].

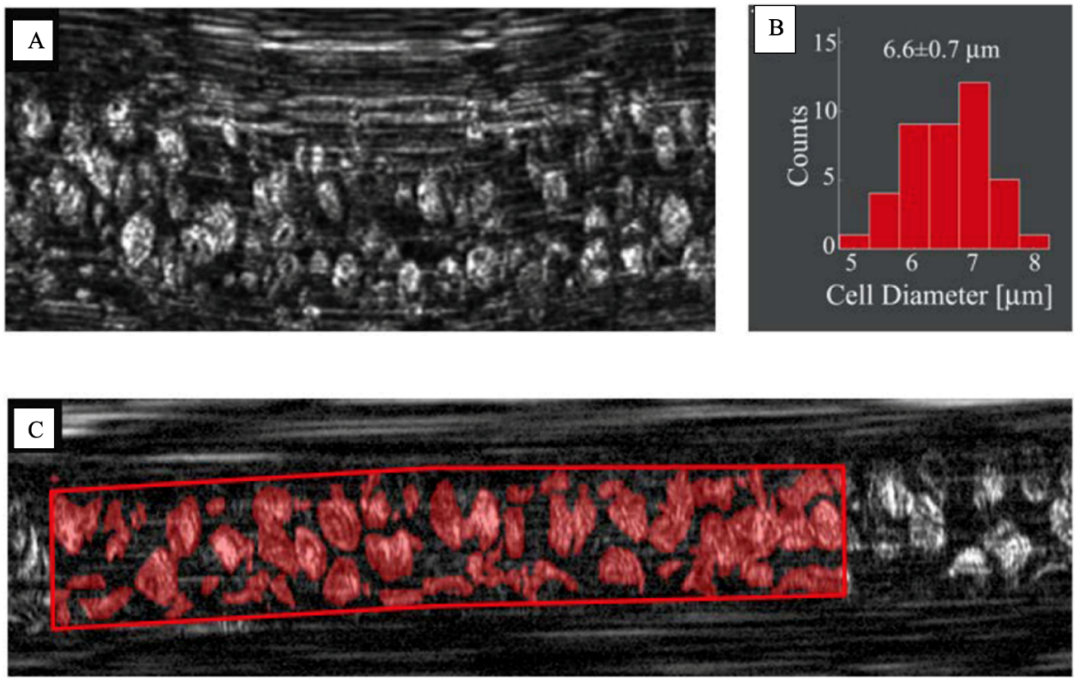

Fig. 2.4. *In-vivo* imaging in microvessels. A) RBC flow in a vessel, B) A histogram showing distribution of RBC diameters. C) calculating the area occupied by RBCs (red regions) to estimating hematocrit levels [36].

2.3.2. Large area SECM

For many screening applications and disease diagnosis, a surface area of about 5-50 cm^2 of organs needs to be imaged with high frame rates. Therefore, the high resolution and improved imaging speed of SECM offer an alternative for conventional RCM [37]. However, the native FOV of SECM is limited to that of the objective lens. To overcome this limitation, several sample translation and image stitching strategies have been introduced. For instance, Kang *et al.* developed a benchtop SECM system to acquire large area images of a biopsy sample of gastroesophageal junctional mucosa of a patient with a history of Barret's esophagus (BE) disease via automated two-dimensional translation of the sample [34] . This study demonstrated the ability of SECM to show subcellular and architectural features of upper GI in large area biopsies. Figure 2.5 demonstrates that the gastric cardia type mucosa can reliably be

differentiated from squamous esophageal mucosa based on the architecture. Also, at higher magnification (panel C), both squamous and columnar cell nuclei can be identified. As shown in this figure, obtained SECM images are highly consistent with the histology images of the biopsy [34]. With the same setup, Yoo *et al.* investigated the count of intraepithelial eosinophils (i.e., a type of white blood cell) in biopsy samples of eosinophilic esophagitis (EoE) patients. Detection of intraepithelial eosinophils is essential for the diagnosis of EoE; therefore, SECM's ability to produce 1-1 matched images of eosinophils with histology was a significant achievement for SECM [38]. However, this study was performed on excised tissue which involves costly, time-consuming and hard to tolerate biopsy procedures. To overcome these limitations, miniaturized SECM endoscopic probes were developed to image large areas [34]. Such miniaturized probes were shown to be able to visualize the cellular features corresponding to esophageal diseases. However, the imaging rate of the abovementioned studies was only 5 kHz, which resulted in a 12-minute imaging time for the entire esophageal [39]. Therefore, Schlachter *et al.* developed the first high speed SECM system with imaging line rate of 100 kHz which can reduce the imaging time to visualize the GI from 12 minutes to 37 seconds [34, 39]. This high-speed SECM system managed to show subcellular features in patients' esophagus, like nuclei of columnar epithelia cells[39].

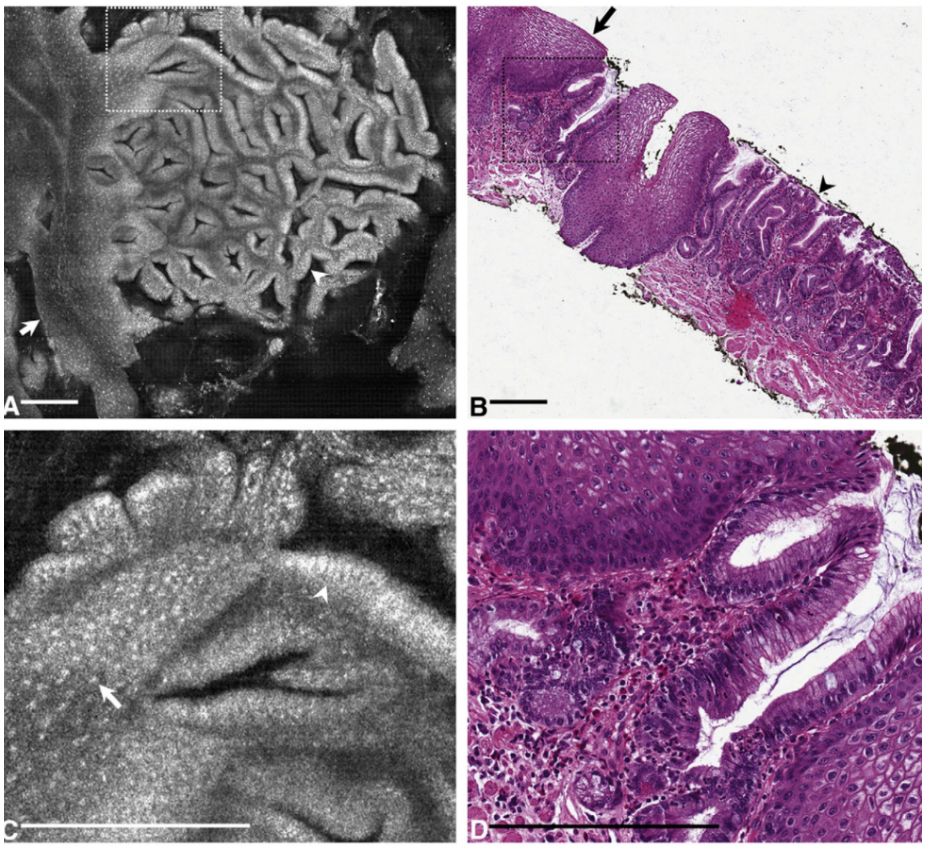

Fig. 2.5. A) Large-area SECM image distinguishes gastric cardia type mucosa (arrowhead) from squamous esophageal mucosa (arrow). B) Histopathologic image demonstrates squamoglandular junctional mucosa. C) High-magnification SECM image identified nuclei of columnar epithelial cells (arrowhead) from squamous cells (arrow). D) High-magnification histopathologic image demonstrates different cell types in the stomach and esophagus. Scale bars represent 250 μm[34].

Promising results in high-speed, large area imaging of clinical samples with benchtop SECM systems as well as miniaturization capability of the system, led to the design and development of endoscopic probes with internal spinning mechanisms for 3D confocal imaging *in-vivo* [40] . To obtain three-dimensional confocal images, a tilted configuration of the objective lens with respect to the tissue surface was designed (Figure 2.6). The tilted angle of the objective lens results in a titled spectrally encoded line in the sample, which can simultaneously illuminate different depths while sample moves with respect to the spectrally encoded line [40, 41] . The tilt angle should be carefully calculated to optimize the range of depth versus the optical

performance [40]. This innovative design opened the door for development of SECM probes and capsules for *in-vivo* volumetric SECM imaging in humans.

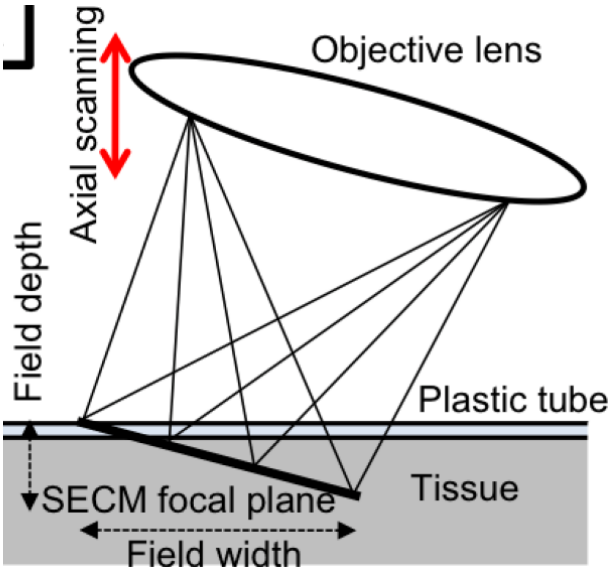

Fig. 2.6. Schematic of the tilted objective configuration and spectrally encoded line in the tissue [40].

The first SECM *in-vivo* probe was initially tested to acquire images of swine esophagus *ex-vivo* and subsequently in imaging of human esophagus *in-vivo* [42]. Large area *in-vivo* images of the esophagus and stomach were taken by helically scanning the probe inside the organ in less than 3 minutes. The developed probes successfully revealed key cellular features and differentiated the architectural structures of the healthy and diseased esophagus. Figure 2.7 shows the developed SECM probe, along with representative SECM images [42].

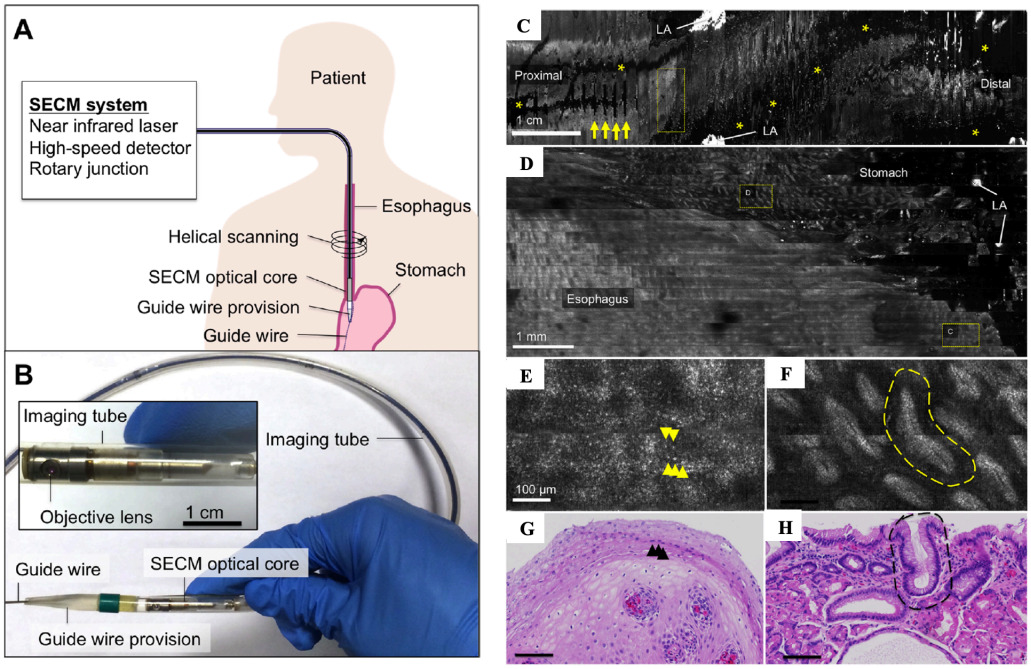

Fig. 2.7. A) SECM endoscopic imaging procedure, and B) photograph of SECM endoscopic probe. Representative *in-vivo* SECM images and histopathologic images of normal esophagus and gastroesophageal junction (GEJ). C) low-magnification view of the entire SECM image, spanning 7.5×2.2 cm; D) magnified view of GEJ at the dotted box in C; E) high-magnification SECM image of esophagus; F) high-magnification SECM image of stomach; (G) and (H) representative images of the esophagus and stomach from the same patient. Arrows in C: zigzag pattern due to peristalsis; asterisks in (C) regions where the SECM probe did not adequately contact the tissue; LA in (C) reflected light from liquid-air boundary; arrowheads in (E) and (G) squamous cell nuclei; and dashed regions in (F and (H) gastric pits. Scale bars in (C–F)=100mm [42].

These advances in development of miniaturized SECM systems led to the development of SECM tethered capsule endomicroscopy (TCE) for un-sedated imaging of human GI tract *in-vivo* [43]. The picture of this capsule is shown in Figure 2.8. The designed capsule has a diameter and length of 7 mm and 30 mm, respectively, which an unsedated human can easily swallow. This study shows success in acquiring large area, cellular-resolution images of the human esophagus that is important for diagnosis and monitoring of diseases such as EoE [41]. Figure 2.9 (A) shows an image taken from a patient with a diagnosis of EoE. Panel B is a

magnified image of the esophagus showing a normal stratified squamous epithelium since it has a uniform pattern. In panel C, highly reflective cells can be seen suggesting the presence of intraepithelial eosinophils. The magnified portions in panel C indicates that the bi-lobed structure of eosinophil nuclei is well resolved. Histopathological images of a biopsy taken from the patient also validated the data acquired by SECM TCE [43].

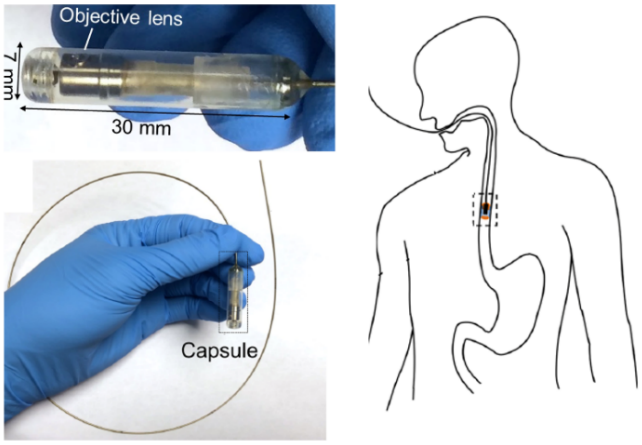

Fig.2.8. Picture of the clinical SECM capsule[43].

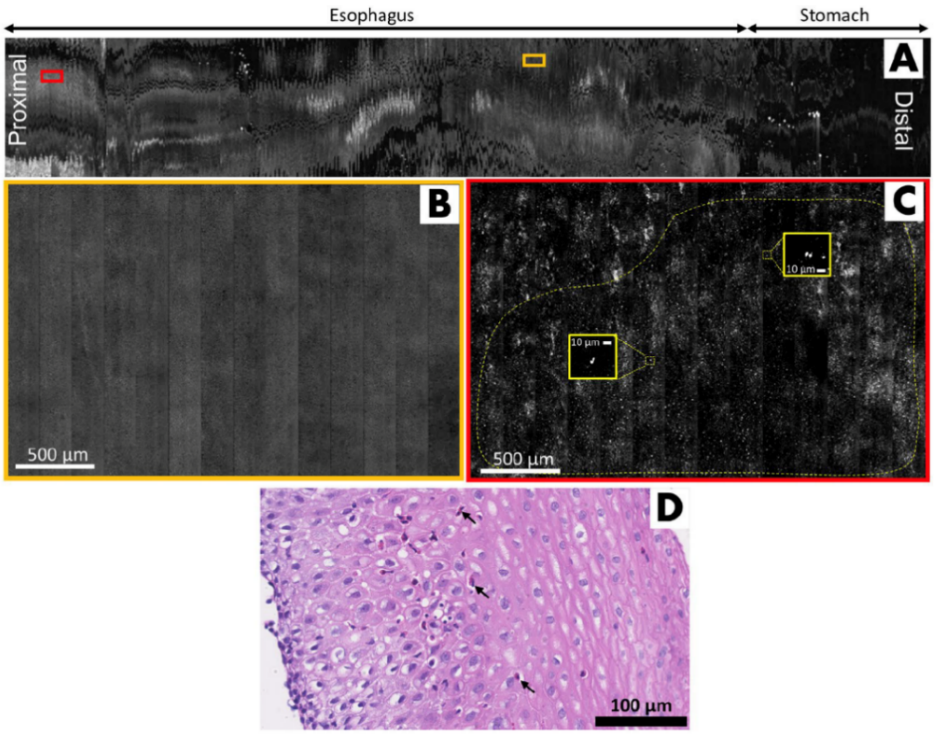

Fig. 2.9. Representative SECM capsule images from an EoE subject, acquired *in-vivo*. (A) Low-magnification view of the entire confocal image, spanning 2.2 cm 25 cm; (B) Magnified portion of (A, orange box) showing homogeneous normal squamous epithelium; (C) Magnified region of (A, red box) demonstrating irregularly distributed highly reflecting cells consistent with intraepithelial eosinophils. The characteristic bi-lobed eosinophil nuclear morphology can be clearly seen (yellow insets); (D) Representative histopathologic image of an esophageal biopy from the same subject confirming the presence of intraepithelial eosinophils (arrows) [43].

2.3.3. Spectrally encoded slit confocal microscopy

The possibility of performing SECM imaging with scan-free confocal optics has also been investigated in both bench-top [44, 45] and low-cost handheld [46, 47] systems (aka spectrally encoded slit confocal microscopy; SESCoM). In SESCoM, a slit acts as the confocal aperture, which will result in focusing different wavelengths of the light into parallel lines in the sample. In such systems, one direction of confocal image is imaged optically while the other direction is imaged through spectral encoding. Therefore, SESCoM offers 2-D confocal images with a 2D spectrometer and without any mechanical scanning [44]. After demonstration of concept, a low-cost handheld SESCoM system was developed for use in resource-poor countries to help disease diagnosis instead of challenging histopathological analysis. In the first handheld device, a smartphone camera was used for the detection; although this low-cost system was successful in revealing cellular features of the skin, the color filter on the phone camera and the short wavelength (590 nm) used for illumination posed some challenges in clearly visualizing the cellular features [46]. This challenges led to utilization of spatially incoherent light sources to reduce the speckle noise [47, 48]. Figure 210 (A) demonstrates successful imaging of numerous keratinized cells; in panel b, the base of the epidermis, a regular honeycomb pattern of cells is observed. Regularly spaced dark openings in panel C are dermal papillae [47].

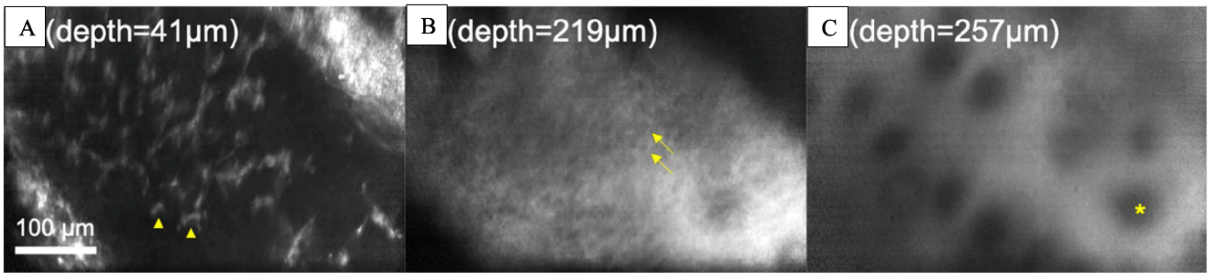

Fig. 2.10. Confocal image of human finger *in-vivo* obtained with the LED-based SESCoM device. A) Epidermis; B) basement membrane; C) superficial dermis. Arrowheads, hyper-keratinization; arrows, basal cells; asterisk, dermal papillae [48] .

To date, SECM mandate has been to offer the resolution and contrast of conventional laser scanning confocal microscopy (LSCM) at higher speed and with miniaturized instrumentation to enable *in-vivo* imaging [31]. Examples discussed in above sections demonstrate the ability of bench-top, probe, capsule, and handheld SECM systems in visualizing tissue features at cellular level. However, compared with LSCM, the presence of speckle noise in SECM images of biological samples is an issue. A double-clad fiber or a higher NA objective lens can be used to reduce the speckle noise [31, 35, 49]. Image speckle can also be minimized through adherence to a multimode detection scheme [49], or the use of spatially incoherent light sources[48]. However, in *C. elegans* research, image speckle is not expected to be a limitation because these nematodes, unlike human tissue, are mostly transparent.

2.3.4. Model organism imaging

SECM previously has been used to image few model organisms such as *Xenopus laevis* and *Danio rerio* [31]. *Xenopus* is an ideal model to study developmental and regenerative processes. Recently the studies are more focused on the development of the heart. *Xenopus* heart has three chambers: the partial atrial septum, which divides the right and left atria, and a ventricle that

gives rise to the truncus arteriosus [29]. Boudoux *et al.* used a SECM system with a FOV of 220 × 220 μm^2, and lateral and axial resolutions of 0.9 μm and 2.5 μm, respectively, to image stage-47 *Xenopus* heart. The representative frames in Figure 2.11 show the spiral valve closing and opening to allow blood flow through it [31]. To the best of our knowledge, SECM imaging of *C. elegans* has not been explored yet.

Fig. 2.11. SECM imaging showing the opening of the spiral valve [31].

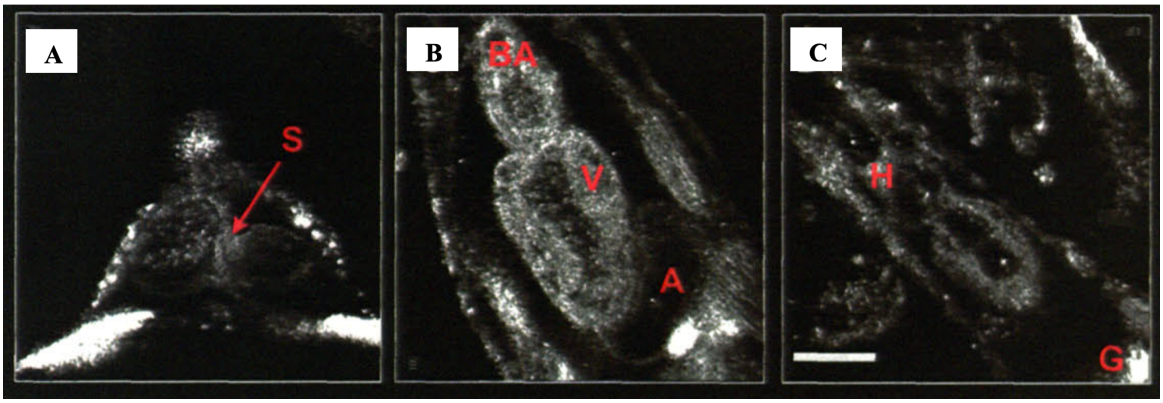

Fig. 2.12. A) Septum (S) create the heart's first chambers at 48-hour post fertilization. B) 5-day and C) 12-day images of the embryo show the fully developed heart. BA-bulbus arteriosus, V-ventricule, A-atrium, G-gut. Scale bar: 50 microns [31].

Chapter 3

Methodology

This section provides detailed information on the experimental setup and methodologies used in this thesis. The chapter opens with the theoretical and simulation optical design of the SECM system. Afterwards, it discusses the performance tests performed to measure the system's performance metrics. Finally, sample preparation and data processing is described.

3.1. Overview of developed SECM system

The schematic of the developed SECM system is depicted in Figure 3.1 (A). Using theoretical equations discussed in Chapter 2 we designed an SECM system for imaging *C. elegans*. The existing light source (center wavelength = 1310 nm; FWHM = 103 nm, Exalos Inc, Switzerland) and spectrometer (Cobra 1300; Wasatch photonics, USA) of our optical coherence tomography system were utilized for development of the SECM system. The spectrum of the laser source is depicted in Figure 3.1. Since the power of laser is sharply decreased at the edges of spectrum, the effective spectral range of our system was determined as 1259-1363 nm (i.e., the full width at half maximum; FWHM).

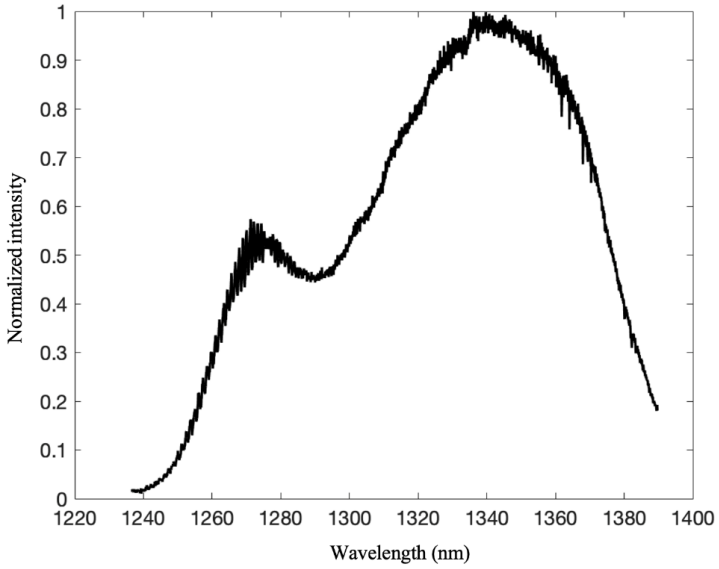

Fig 3.1. Spectrum of the laser source.

In developed SECM system (Figure 3.2), the light from the laser source travels through a single-mode optical fiber (SMF-28), then it passes through an optical attenuator (A). Optical attenuator is a device to manually vary the attenuation of the light in the fiber. It has a lens to collimate the incoming light, and a manually adjustable window, and a second collimator lens for coupling the attenuated light into the output fiber. This device allows us to change the coupling efficiency between input and output fibers until the desired attenuation is obtained. Following the attenuator, light enters the first port of an optical circulator (C). Optical circulator is a three-port device, which allows the light to travel only in one direction. The light entering port one exists via port two with minimal loss; and the light entering from port two exits from port three with minimal loss. In the imaging arm, the light from port two of circulator is collimated (via L1) to a 3 mm spot size and reflected off a 1-D galvanometric (galvo) mirror scanner (Thorlabs Inc, USA). Galvo mirror consists of a galvanometer-based scanning motor with a mirror mounted on a shaft and a detector to provide positional feedback to the control board. A programmable voltage source (DAQ card; National Instruments) is used to move the

galvo via an RF signal. After the mirror the beam is directed to a transmission diffraction grating (HD 1145 l/mm: Wasatch Photonics, USA). The angle of incidence on the grating is optimized to be 48.6° (Littrow's angle for 1310 nm) to maximize the first order diffraction efficiency. Through a custom-made telescope (L2 and L3) the diffracted beam fills the back aperture of a long working distance NIR objective lens (Mitutoyo, Plan Apo NIR 20X/0.4 NA, and 50X/0.42 NA) which, in return, focuses different wavelengths of the laser source on a line (aka. spectrally encoded line; See Figure 3.2(A) inset). The reflected light from the sample travels back the same optical path and couples to the optical fiber and enters the second port of the optical circulator and then is sent to the spectrometer (Cobra 1300; Wasatch photonics) via the third port of the circulator for analysis. The developed SECM system can instantaneously image the confocal line with a speed of up to 147,000 times per second. To form 2D confocal images, a custom-made program was developed in the LabVIEW environment to synchronously move the galvanometric mirror to produce 200 μm × 600 μm images with 20X objective at an imaging speed up to 300 Hz. To ensure accurate and repeatable positioning of the sample in the confocal plane, the sample platform was equipped with three compact motorized translation stages (Thorlabs Inc., USA) with minimum movement step size and bidirectional repeatability of 0.05 μm and 1.6 μm, respectively.

Two sets of objective lenses, 20X and 50X magnification, were used in the experiments. 50X objective lens provides better resolution and higher magnification at the cost of lower power and smaller field of view. With respect to the objective lens used in our system, it should be noted that dry objectives are generally more prone to spherical aberrations and image degradation with the increase in imaging depth than water immersion objectives; however, the significantly longer working distance of the dry objective used in our system is expected to

facilitate better downstream integration of SECM in microfluidic platforms that often contain multiple bulky components on their interrogated surface (e.g., inlets, outlets, tubes and micro pumps). Sections below explain how we designed and selected the optical components used for building the SECM system.

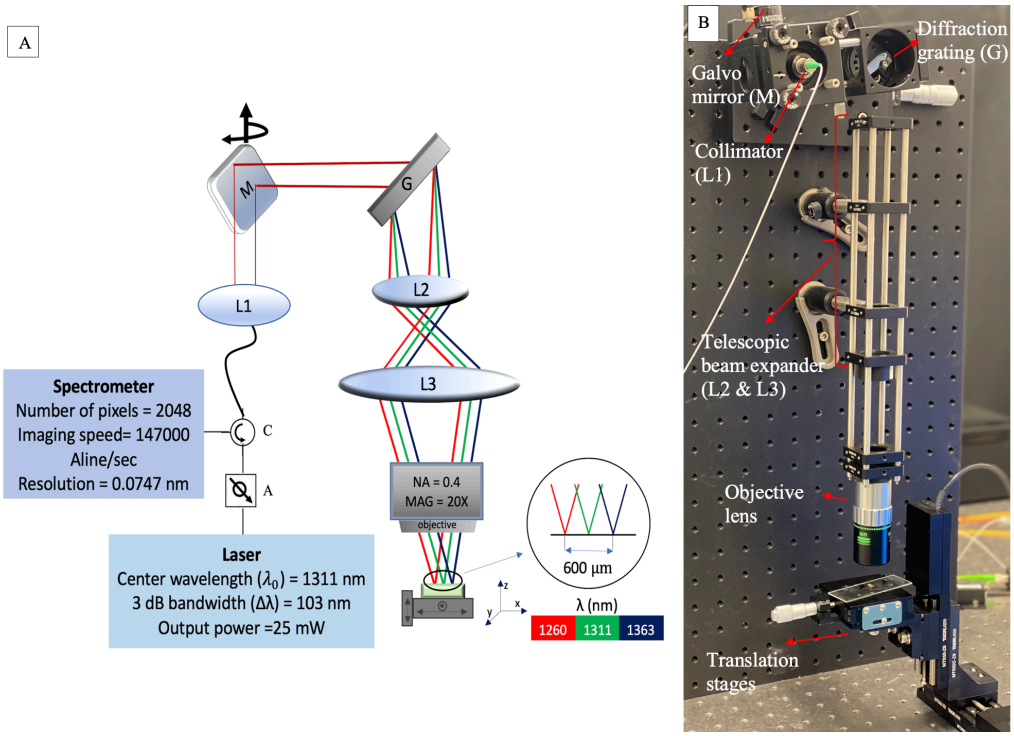

Fig. 3.2. A) Schematic, and B) picture of the SECM system. A: attenuator C: circulator, L1: collimator, M: galvanometer mirror, G: diffraction grating, L2, L3: telescopic beam expander, (b) Schematic of the APL-OP01 patterns; reprinted with permission.

3.2. Optical design

After the conceptual design of the system, we used OpticsStudio Zemax to find the optimized spacing between optical components of the system. We used Zemax's native merit function for minimizing the point spread function of the imaging system. Once optimized, we measured $\Delta\theta$ from Zemax simulation because the theoretical equation 2.8 is not applicable to SECM systems like ours with the telescope after the diffraction grating (compare Figures 2.1 and 2.3). That is,

if we use equation 2.8 for our system a $\Delta\theta$ value of 5.7° will be predicted. However, since in our system the telescopic beam expander is designed to be after the diffraction grating the Zemax ray tracing predicts a $\Delta\theta$ value of 3.5° (Figure 3.3). Once the correct $\Delta\theta$ was found, using equation 2.7 and the focal length of f=10 mm, theoretical FOV was calculated as 611 μm in the spectrally encoded direction.

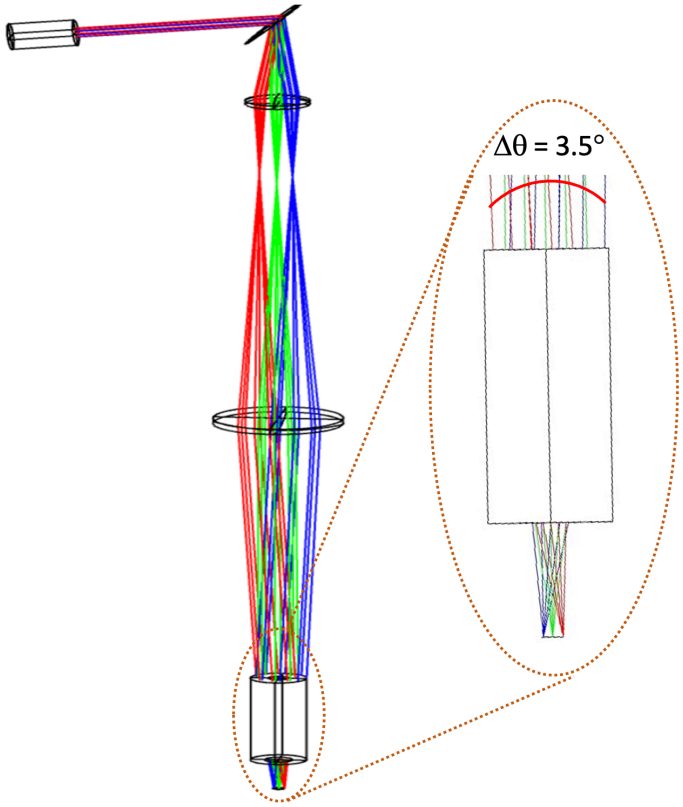

Fig. 3.3 Zemax drawing, showing spectrally encoded line. After the grating angular deviation of each wavelength is different, so each wavelength will focus on a specific spatial location after the objective lens. Red, green and blue line refer to 1363 nm, 1311 nm and 1259 nm, respectively.

As mentioned in the previous chapter, the lateral resolution of a SECM is governed by three factors [31] :

1) The focal spot size of the objective lens
2) The spectral resolving power of the diffraction grating

3) The spectral resolution of the spectrometer

Based on Rayleigh criterion for a confocal system ($0.56\lambda/NA$), for a wavelength of 1310 nm and a 0.4 NA objective lens the theoretical focal spot size of our system (δx) is 1.83 μm. With respect to equation 2.6, with $\delta x = 1.83$ μm and FOV = 611 μm, our SECM system theoretically yields 333 resolvable points across the spectrally encoded line. The spectral resolution of the system ($\delta\lambda_g$), using the grating period and beam size of our system, is calculated by equation 2.4 to be 0.2285 nm. Using equation 2.5, this spectral resolution of the diffraction grating results in 450 resolvable points, which satisfies the preferred condition for oversampling in the spectrally encoded line [32, 33]. In order to achieve Nyquist sampling, we need to sample at least 900 pixels per spectrally encoded line, which is achievable by the 0.075 nm spectral resolution of the spectrometer [39]. Given above theoretical calculations, the lateral resolution of our system is limited by the optical resolution of the system (i.e., 1.83 μm leading to 333 resolvable points along the 611 μm FOV) [31].

Using equation 2.3 for the 20X/0.4 NA objective lens, the axial resolution of the system was calculated to be 7.4 μm.

Table 1 depicts the anticipated parameters of our designed SECM system. The highlighted cells are parameters which are fixed by the specifications of optical components. Based on these parameters, the designed SECM system offer satisfactory resolution and FOV of imaging *C. elegans.*

Table 1: parameters and their values in SECM system

Parameter	λ (nm)	Δλ (nm)	NA	f (mm)	D (mm)	δx (μm)	δz (μm)	Λ (mm)	θ_l	$\Delta\theta$	FOV (μm)	$\delta\lambda_g$ (nm)
value	1311	103	0.4	10	5.05	1.83	7.4	0.87	48.6°	3.5°	611	0.22

We also studied system's aberration in Zemax to come up with an optimal magnification value of the beam expander. In an ideal system, a flat ray fan at focus indicates the absence of aberrations. Figure 3.4 depict the predicted ray fans of our system in spectrally encoded and perpendicular to spectrally encoded directions when using a 3X beam expander. At this magnification, we found the system to theoretically yield minimal aberrations (note flat lines in Figure 3.4). Consequently, we built a 3X beam expander in our system using two aspheric lenses with 5 mm and 15 mm focal lengths, respectively. Scanning of the spectrally encoded (SE) line, with movement of galvo can also be studied with Zemax. Figure 3.5 shows the left, right and center position of the SE line at the corresponding galvo mirror positions.

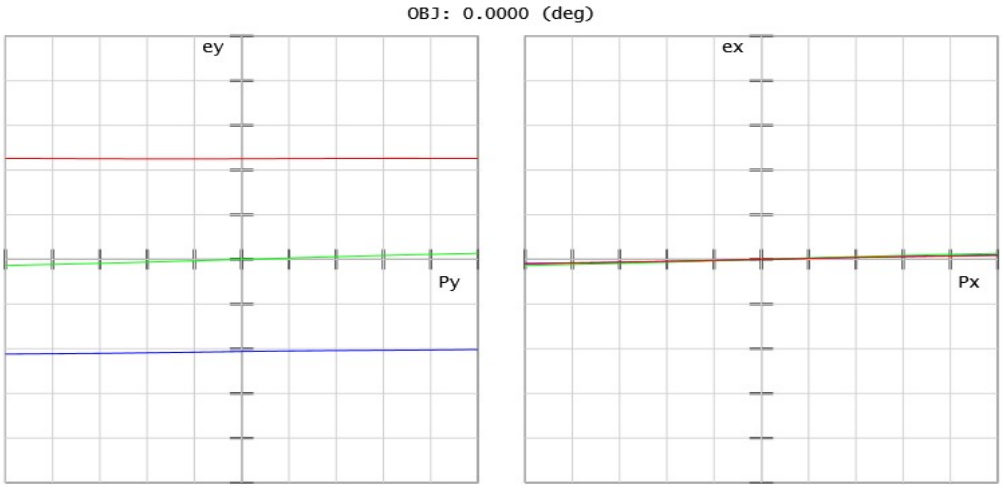

Fig 3.4. Ray fan diagram of the SECM showing the aberration. Red, green and blue line refer to 1363 nm, 1311 nm and 1259 nm, respectively.

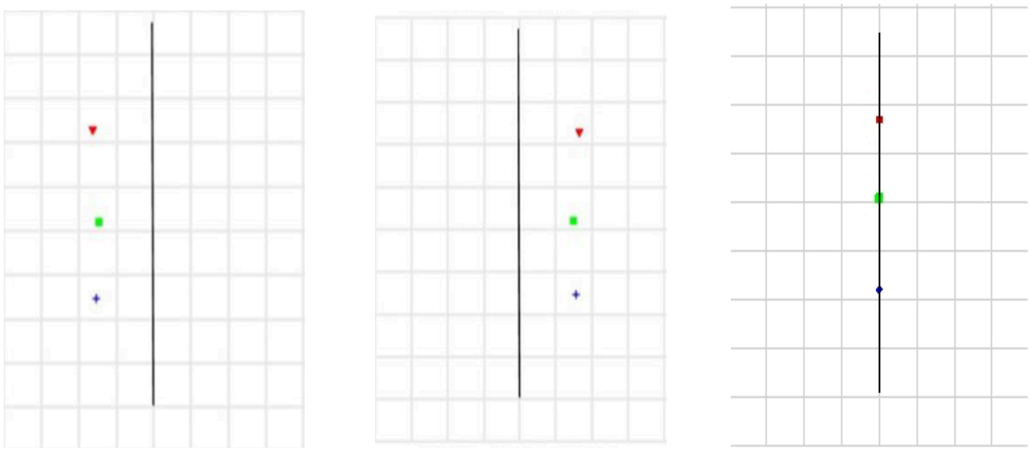

Fig. 3.5. Simulation of the beam scanning by the galvanometer mirror in Zemax. Red, green and blue color refer to 1363 nm, 1311 nm and 1259 nm, respectively.

3.3. Performance tests

Following above theoretical and numerical works, we designed our SECM system, procured the required components, built system hardware, and developed system software. However, the actual performance of any optical system deviates from the theoretical predictions due to the aberrations caused by optical components and the misalignments of the system. Therefore, it was essential to also measure the performance metrics of our SECM system. To do so, we carried out standard characterization tests which will be discussed in this section.

First to measure the pixel size of the system, we used a standard microscopy calibration slide (Bioimager Inc. Canada). The line spacing in the finest section of this slide is 0.01 mm and the LabVIEW program allows to count the number of pixels between two reflective lines. Therefore, by dividing the 0.01mm spacing by number of pixels we found the image pixel size in spectrally encoded and galvo scanning directions.

Next to evaluate the optical performance of the SECM system, several benchmark tests were carried out. Line distortion, lateral resolution, and point spread function were assessed by

imaging the corresponding segments of the Arden validation phantom (APL-OP01, Arden Photonics; Figure 3.6) [28]. These segments are comprised of 8 layers of reflective line patterns; the first layer is located 100 μm below the top surface, and axial spacing between the layers is 75 μm. The distortion pattern has 100 × 100 μm^2 square reflective grids. The FOV was quantified using this pattern. In the point spread function, there are series of lines in each layer separated by 150 μm. Each layer is laterally offset by a 25 μm distance from the next layer. The lateral resolution pattern is comprised of groups of 11 reflective lines with varying lateral spacing. Each line in this pattern is separated laterally from the next by a distance, starting at 1 μm and increasing by increments of 1 μm. Once the group and line numbers of line pairs that just blur together are identified, a reference equation (Equation 3.1) is used to estimate the lateral resolution:

$$line\ spacing = 11(m-1) + n \tag{3.1}$$

In this equation m is the group number and n indicates the number of the line within the group.

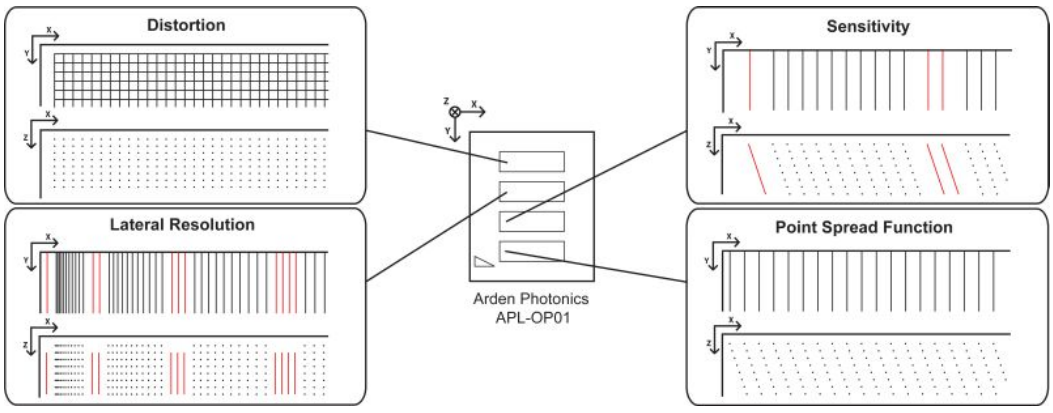

Fig. 3.6. Schematic of the Arden phantom APL-OP01

The lateral resolution offered by the Arden phantom is an estimation. To precisely measure the lateral resolution of the system we used the line spread function method, which is the

response of the system to a thin reflective line across the sample. The FWHM of the derivative of the intensity profile across the reflective line determines the lateral resolution of the system.

To measure system's axial resolution, a mirror was scanned through the focus with a 0.5-μm step size. The full width at half maximum (FWHM) of the intensity profile was considered as the axial resolution of the SECM system.

3.4. *C. elegans* strains, maintenance, and synchronization

Wild-type (WT) (N2) as well as MT2124, MT1082, CB61, and CB648 strains were obtained from the *Caenorhabditis* Genetics Center (University of Minnesota, Minneapolis, MN, USA) (Table 2). The maintenance and synchronization were done by advanced center for microfluidic technology and engineering (acute; let by Prof. Rezai) in York University. They were grown on standard nematode growth media (NGM) agar plates (6 cm in diameter Petri dishes) prepared with *Escherichia coli* OP50 as a food source at room temperature (~ 22 °C) [50]. A pre-sterilized cabinet is used to keep the worms safe, also it has been thoroughly cleaned every day to eliminate any chance of contamination. A freshly prepared Luria Broth (LB) media (10 g bacto-tryptone, 5 g bacto-yeast, and 5 g NaCl in 1 L distilled water) was inoculated with a single OP50 colony and cultured overnight in a thermal shaker incubator at 37 °C. The NGM plates were seeded with 100 μL of the bacterial culture and left to dry overnight at room temperature. *C. elegans* maintenance was performed under Biosafety protocol Number 02-19 issued by York University's Biosafety Committee to Professor Pouya Rezai.

All experiments were conducted with age-synchronized worms using the Alkaline hypochlorite treatment [51]. Briefly, well-fed gravid adult worms were washed off plates in a 15 mL Eppendorf tube using M9 buffer (3 g KH_2PO_4, 6 g Na_2HPO_4, 5 g NaCl, and 1 ml 1 M

$MgSO_4$ in 1 L distilled water). Then, the worms were treated for 10 minutes according to Porta-de-la-Riva *et al.* protocol [51], using a commercial bleach solution (3.875 mL double-distilled water, 125 µL NaOH, and 1 mL commercial bleach). Following the treatment, the eggs were collected and incubated in 1 mL M9 buffer and allowed to hatch overnight. The hatched L1 larvae were plated on freshly prepared NGM and allowed to grow to the gravid adult stage, except for starved worms. To obtain starved worms, gravid adult worms were manually picked to a freshly prepared unseeded NGM plate until starvation. For imaging, worms were individually picked and fixed between two microscope coverslips with a droplet of M9 containing 25 mM of sodium azide [52]. Sodium azide has been extensively used as an anesthetic for *C. elegans* to slow or stop its movement for high-resolution imaging. The worms generally stopped moving within a minute or two.

Table 2: *C. elegans* strains used in his study.

Strain	Genotype	Description
N2	WT Bristol	Wild type
MT2124	let-60 (n1046)	Multivulva phenotype [52].
MT1082	egl-1 (n487)	Egg-laying defective, Retains late-stage eggs [53].
CB61	dpy-5 (e61)	Strong dumpy; early larvae non-Dpy [54].
CB648	vab-3 (e648)	Notched head [55].

3.5. Data processing

In each test prior to acquiring the images, we recorded the background signals in absence of the sample. For the purpose of data processing first the recorded background is subtracted from each image to remove the background noise.

For the purpose of microorganism imaging, we put the samples between a glass slide and a coverslip. This arrangement can cause periodic interference patterns in the images (Figure 3.7.(A)). In order to remove the periodic dark and bright patterns, periodic noise removal in the spatial frequency domain (aka. K-space) can be employed. By transferring the image to the Fourier domain, the periodic noise can be distinguished from the desired image as the two symmetric bright dots around the center, blue arrows in Figure 3.7 (B). Therefore, in MATLAB we can easily compute the fast Fourier transform (FFT) of the images (Figure 3.7(B)), remove the undesired components (Figure 3.7(C)), and then by using the inverse fast Fourier transform (iFFT) rebuild the cleaned-up images (Figure 3.7 (D)).

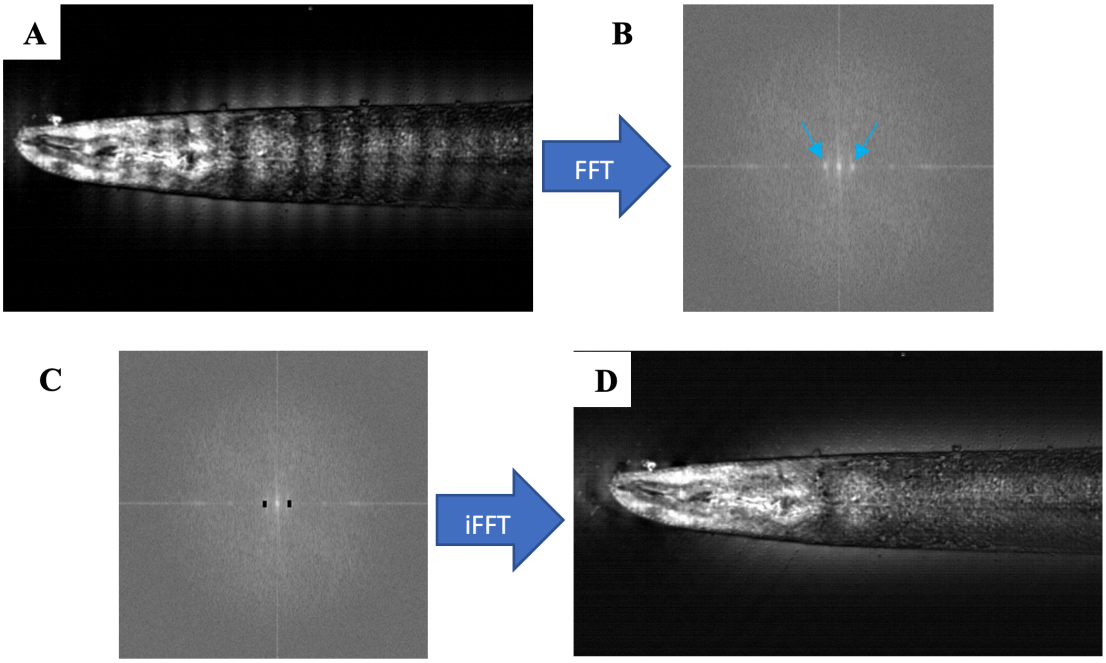

Fig. 3.7. (A) Original image, (B) Fourier transform, (C) filtering in Fourier space, (D) filtered image.

Chapter 4

Results and Discussion

This section presents and discusses the results of the system characterization experiments and the outcome of imaging WT-N2 and mutant *C. elegans* with the developed SECM system.

4.1. Characterization tests

As mentioned in Chapter 3, using the Bioimager calibration slide the pixel size in both galvo scanning and spectrally encoded direction, were measured to be 0.4 µm and 0.2 µm with 20X and 50X objective lenses, respectively.

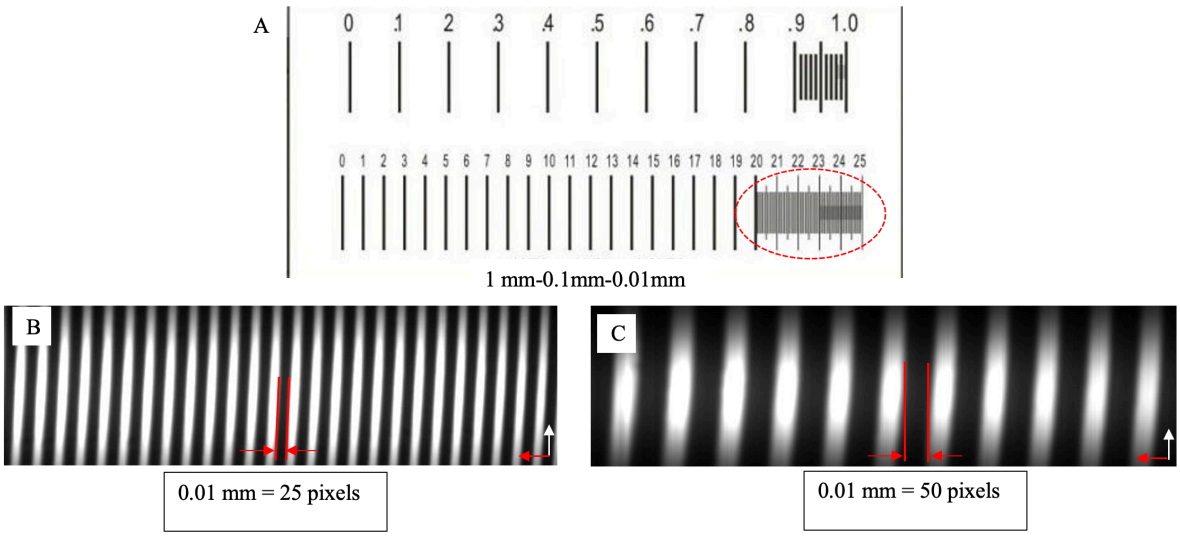

Fig 4.1. A) Bioimager calibration slide. SECM images of the red circle section with A)20X and B) 50 X objective lens.

4.1.1. Distortion pattern

The SECM image of the first layer of Arden phantom's distortion pattern is depicted in Figure 4.2(A); this pattern is imaged with a 20X/0.4 NA objective lens. While no obvious distortion is observed in the spectrally encoded direction, a slight curvature of lines can be seen in the galvo scanning direction. This distortion can be related to non-optimal scanning of beam over the back aperture of objective [56]; however, the induced distortion is minimal (less than 2 μm shift over a 100 μm-line) and not expected to be significant when imaging *C. elegans*. The 3D render of all eight layers can be seen in Figure 4.2(B). It demonstrates the system's ability to image layered grid patterns spanning 600 μm in depth without any noticeable distortion. Using the distortion pattern's 100 × 100 μm^2 cell size as a reference, the maximum field of view with the 20X objective in the spectrally encoded and galvo scanning directions were measured as 600 μm and 200 μm, respectively. The measured 600 μm optimal length of the spectrally encoded line corresponds to the FWHM of the light source and was theoretically calculated as 611 μm in Chapter 3. The small difference between the estimated and measured values can be due to small misalignment of telescope lenses leading to slightly smaller angular deviation of wavelength extremities ($\Delta\theta$) at the back aperture of the objective lens.

Figure 4.2(C) depicts the distortion pattern imaged with 50X/0.42NA objective lens. There is no line distortion in case of using 50X/0.42 NA in spectrally encoded direction, and distortion in the galvo scanning direction is also negligible. Based on the distortion pattern image, the maximum FOV with the 50X objective in spectrally encoded direction and galvo scanning direction is 200 μm and 50 μm, respectively. While using the 50X objective lens results in

improvement of resolution, the optical power, FOV, and image contrast are significantly reduced. Therefore, we believe that the 50X objective is more suitable for imaging the cross section of *C. elegans* (~50 μm) and the 20X objective is more suitable for imaging the nematodes laterally.

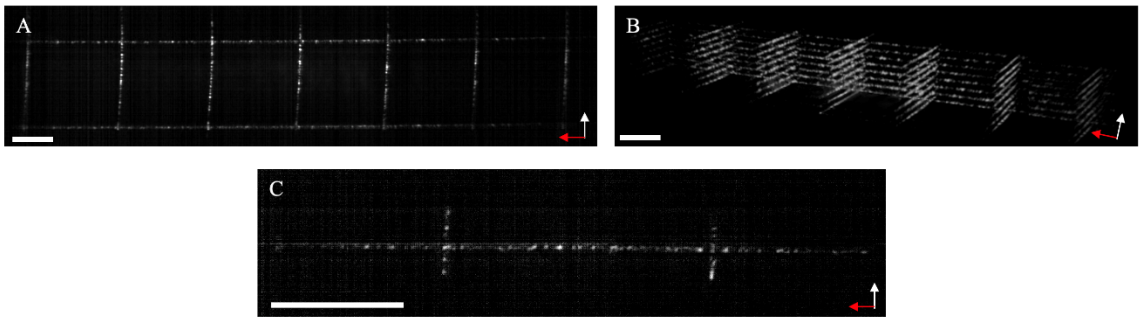

Fig 4.2. (A) SECM image of the first layer of distortion pattern, and (B) 3D render of the patterns in distortion group in all the layers, taken with 20X objective lens C) Distortion pattern obtained by 50X objective lens. Scale bar=50 μm. White and red arrows indicate galvo scanning and spectrally encoded directions.

4.1.2. Lateral resolution

To measure the lateral resolution, the first group of the resolution pattern of the Arden phantom, which contains the minimum line spacing, was fitted to the FOV of the system. Figure 4.3 (A) and (B) show the pattern acquired with 20X objective lens. The images of panels A and B show that lines 1 and 2 cannot be reliably differentiated from each other but the separation of line 2 from line 3 can clearly be recognized in both spectrally encoded and galvo scanning directions. As such, based on Arden phantom reference equation (Equation 2.9), system's lateral resolution is estimated to be ~2 μm. The FWHM of the LSF measured to be 2.08 μm and 2.17 μm in the galvo scanning and spectrally encoded directions, respectively (panels C and D in Figure 4.3). The lateral resolutions measured with LSF method are consistent with the estimated value from Arden phantom. However, the measured lateral resolution is inferior to the one

estimated from Rayleigh criterion (e.g., 2.08 µm vs 1.83 µm), leading to number of resolvable points in the spectrally encoded direction smaller than the theoretical value (600 µm/2.08 µm= 288 points vs 333 points). We hypothesize that the difference between estimated and experimental values is due to the aberrations introduced by the objective lens.

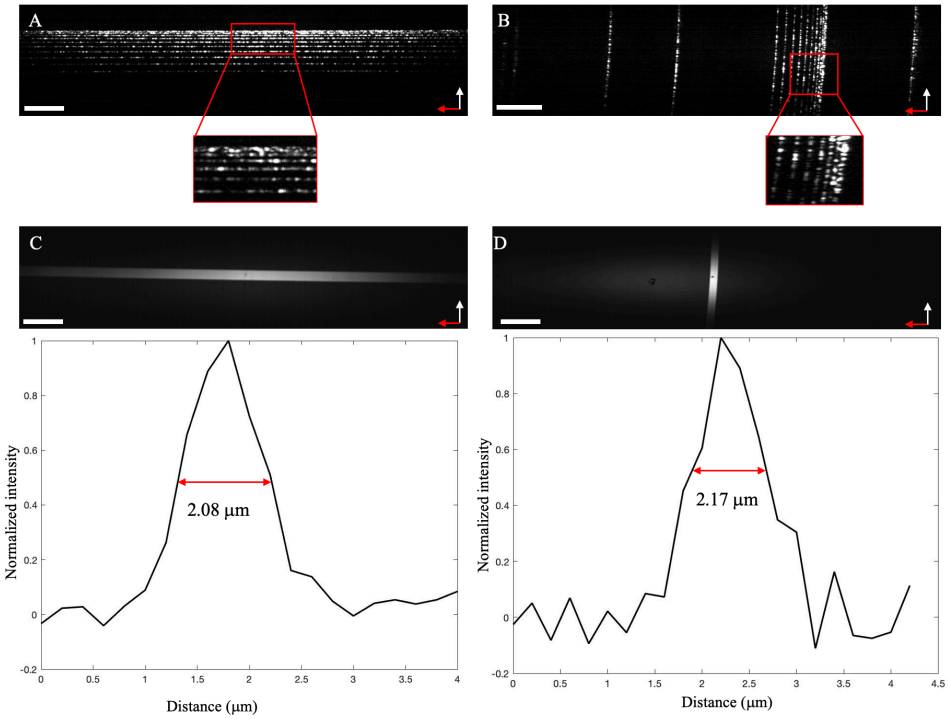

Fig. 4.3. First group of the lateral resolution pattern of the APL-OP01 phantom in (A) galvo scanning and (B) spectrally encoded directions. Scale bars =50 µm. FWHM of the LSF in (C) galvo scanning and (D) spectrally encoded. White and red arrows indicate galvo scanning and spectrally encoded directions.

Figure 4.4 (A) and (B) depicts images of the Arden phantom acquired with the 50X objective lens. With the 50X objective, we can differentiate the line 2 from the first line of the Arden pattern in the first group; therefore, the lateral resolution is estimated to be less than 2 µm. The measured values by FWHM of the LSF have also confirmed the resolution to be 1.42 µm and 1.57 µm in spectrally encoded and galvo scanning directions, respectively (Figure4.4(C) and

(D)). These values still slightly differ from the 50X theoretical value of 1.7 µm, perhaps due to lens aberrations.

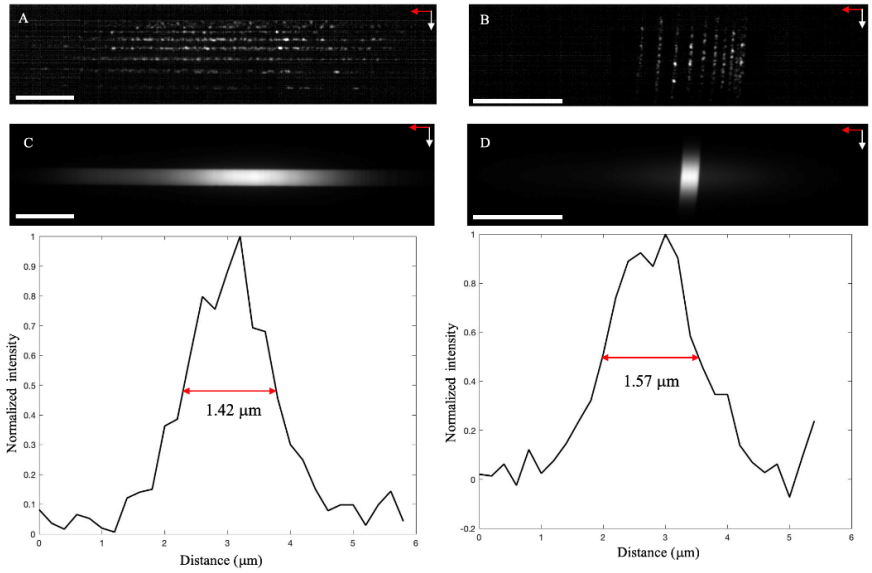

Fig. 4.4. First group of the lateral resolution pattern of the APL-OP01 phantom in (A) spectrally encoded and (B) galvo scanning directions obtained by 50X objective. Scale bars =50 µm. FWHM of the LSF in (C) galvo scanning and (D) spectrally encoded. White and red arrows indicate galvo scanning and spectrally encoded directions.

4.1.3. Point spread function

Figure 4.5(A) shows the measured PSFs along the depth of the phantom taken by the 20X objective. The PSF pattern is often used to evaluate the degradation of lateral resolution along the depth due to aberrations [57]. PSF depends on the wavelength of the light and NA of the objective lens. Comparison of the FWHM of the normalized curves shows that moving the confocal image plane 600 µm in glass medium yields minimal deterioration of PSF. The average FWHM of PSF was measured as 2.17±0.3 µm which is consistent with measurements made with the lateral resolution pattern. Panel B shows the 3D construction of the layers of the PSF pattern taken with 20X.

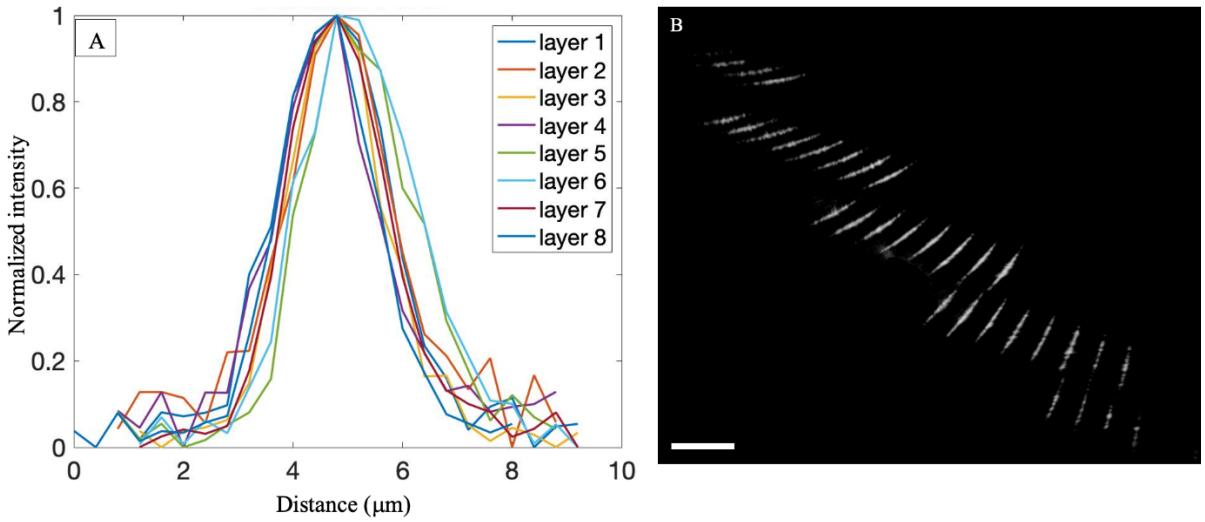

Fig. 4.5. A) Normalized PSFs of the eight layers of the APL-OP01. B) 3D reconstruction of the PSF pattern

4.1.4. Axial resolution

Figure 4.6(A) depicts the axial response of the SECM system using the 20X objective lens. The FWHM of the axial response curve was measured to be 10 μm. Figure 4.6(B) depicts the axial resolution in case of using a 50X objective lens. FWHM of the intensity profile is 8.2 μm. The theoretical values for axial resolution were calculated to be 8.2 μm and 6.7 μm for 20X and 50X objectives, respectively. The spherical aberration of the lens can be responsible for the difference between theoretical and experimental values of the axial resolution.

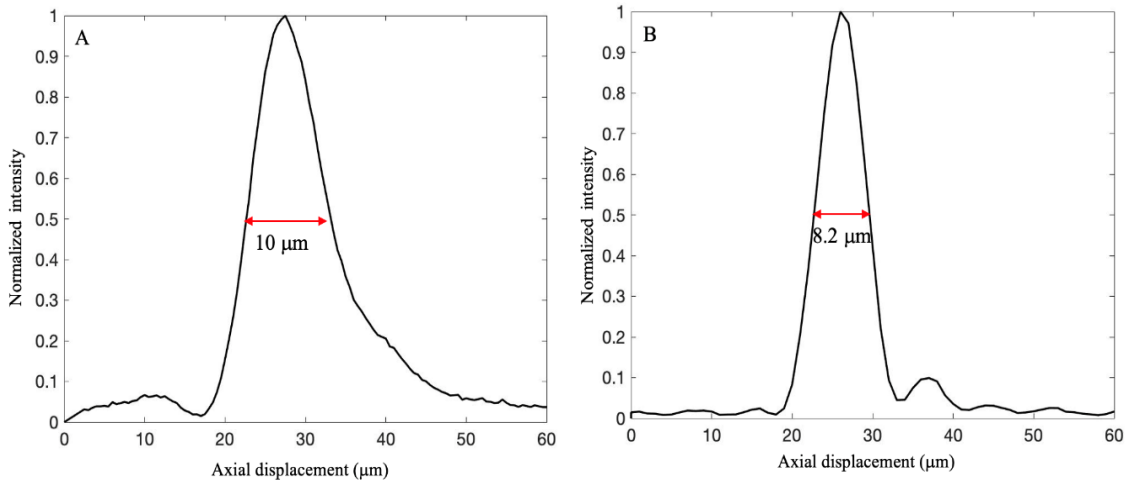

Fig. 4.6. System's axial response obtained by scanning a mirror through the focus of the (A) 20X objective and (B) 50X objective.

4.2. Adult WT *C. elegans* imaging

Based on the results of the optical performance of the developed SECM system (e.g., resolution and FOV) and the existing technological gap in high-throughput confocal imaging of *C. elegans*, this model organism appears to be a perfect fit for SECM imaging. After being satisfied with the system optical performance, gravid worms were imaged with the system to determine the SECM ability in resolving internal organs of the worm. Since the length of the worms are longer than the length of the spectrally encoded line, to accommodate the extended length of the entire worm, image stitching was performed. Figure 4.7 depicts images of adult WT *C. elegans*. Preliminary images of the gravid worms reveal not only the overall geometry and size of the worm, but also resolve key internal organs. For example, in the pharyngeal region, procorpus, metacorpus, isthmus, and posterior bulb can be seen in panel A. High-speed and high-resolution visualization of these organs is critical for a spectrum of disease models. For example, the contractions in pharynx are important in studies related to feeding behavior of *C. elegans* [8].The regulation of food intake can determine the rate of growth, also food related

misbehavior can cause disorders such as obesity, type 2 diabetes, cardiovascular diseases and some cancers. Based on the similarity between genome of *C. elegans* and human, *C. elegans* has emerged as a powerful model to study food-related behaviours. Intestine is another interesting organ of the worm that can clearly be resolved in the body, extending from the head to the gut. Imaging the intestine is vital in disease studies related to fat storage disorders, diabetes, and metabolic syndrome [58, 59]. Factors controlling energy metabolism are conserved between mammals and *C. elegans* providing a strategy to delineate the molecular pathways that lead to metabolic disorders[58] .

In the middle part of the worm, the uterus is located where the eggs are stored and deposited through the vulva. Vulva development is widely studied in studies related to deregulation of cell growth and division which lead to tumor development in mammalians. The let-60 gene plays an important role in formation of vulva. Gain of function (GF) mutations in let-60 can result in multivulva phenotype, which are similar to mutations causing dysregulated cell division in human. On the other hand, partial loss-of-function mutations in let-60 gene lead to a vulvaless phenotype [60]. Panel B shows SECM image of *C. elegans* with multiple eggs inside their bodies. This image demonstrates, the resolution and the contrast of the system are sufficient to reveal the eggs and allow the operator to count the numbers of them inside the body of the worm. The imaging depth in this image was chosen in the way to show the eggs. In the absence of food *C. elegans* retains fertilized eggs in the body and stops egg laying. Also, different food source can have different effect on egg-laying behavior of the worms, which can be studied by egg-in-worm assay [61]. Panel C shows the SECM image of a young adult *C. elegans*. The SECM image, clearly, resolves key organs in the head region such as mouth, procorpus, metacorpus, isthmus, and posterior bulb as well as other body organs such as gonad

and a developing vulva. The length of this worm is measured as 860 μm with a diameter of ~ 50 μm which is smaller than the adult *C. elegans* of previous panels, as expected. Figure 4.7 D depicts a starved worm with several L1 worms inside the body (blue arrowheads). Parent's pharyngeal region, intestine, and vulva are also visible in this image. Moreover, this image verifies that SECM is even capable of resolving the geometry and some details inside the worms in early stages. The dark region (white arrowhead) is a stitching artifact and not from the sample. With respect to results from non-fluorescent techniques discussed in chapter one, the resolution and contrast of SECM images are much superior to those of the conventional modalities.

System evaluation tests in Chapter three showed that 50X objective can provide a better resolution. Figures 4.8 show high resolution SECM images of the eggs and vulva of an adult *C. elegans*, acquired with the 50X objective lens. The higher magnification allows for resolution of internal cellular constituents of the eggs, albeit at the cost of smaller FOV.

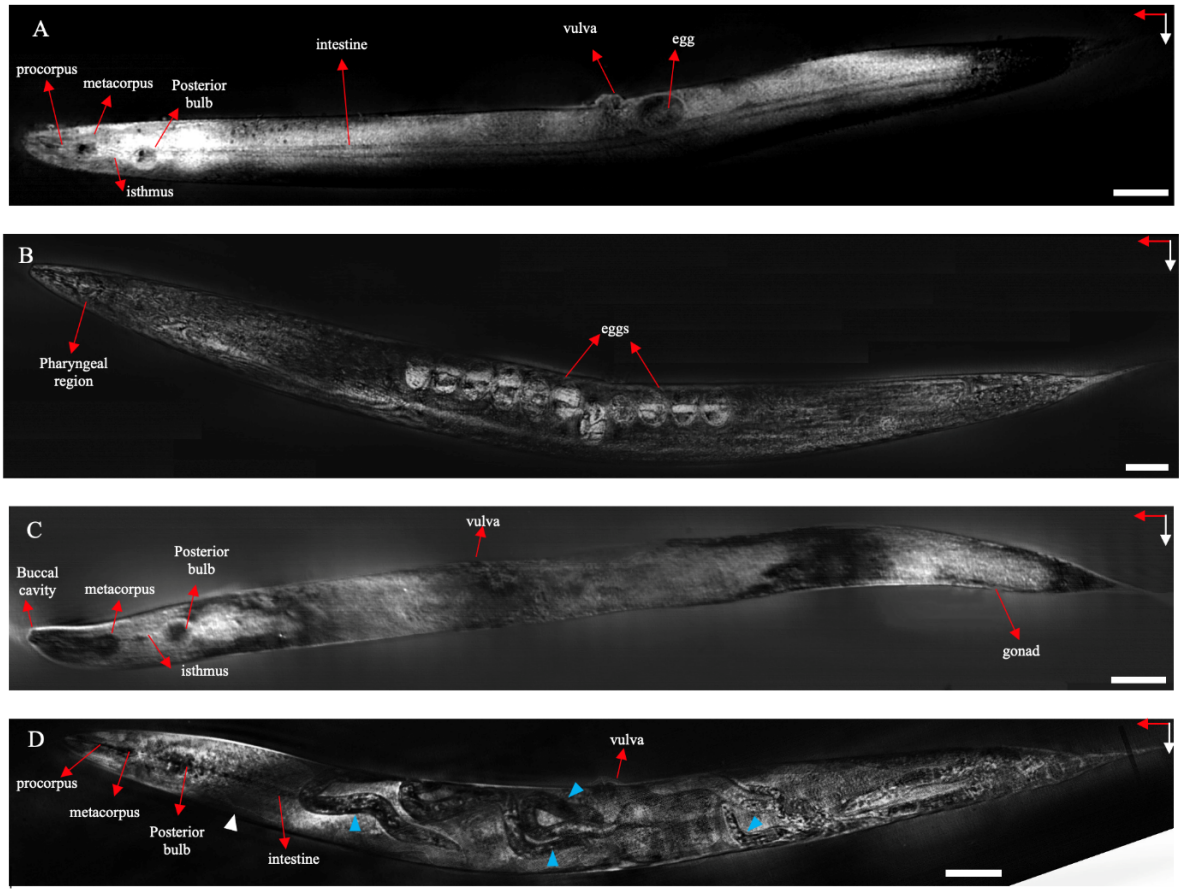

Fig. 4.7. SECM images showing different internal organs of (A) and (B) adult *C. elegans*, (C) *C. elegans* in the young adult stage, (c) worm-bagged *C. elegans* with larvae inside it (blue arrowheads). Scale bar =50 µm. White and red arrows showing galvo scanning and spectrally encoded direction respectively.

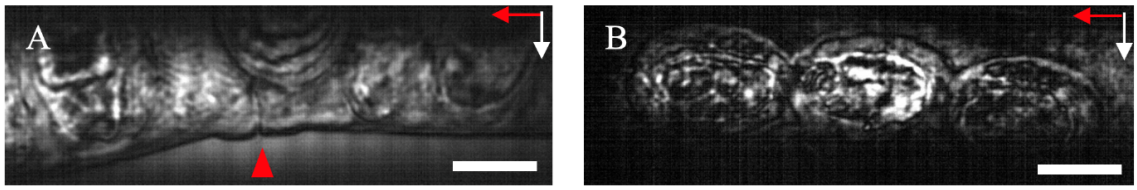

Fig. 4.8. High magnification images of (A) vulva (red arrowhead) and (B) eggs of an adult *C. elegans* obtained with 50X objective. Scale bar =50 µm. White and red arrows showing galvo scanning and spectrally encoded direction respectively.

One of the important features of the SECM is optical sectioning ability of the system while maintaining the high speed. To confirm system's optical sectioning ability, a gravid adult worm

was axially scanned in 15 µm steps. Figure 4.9 depicts four axial image slices of the *C. elegans* head demonstrating appearance and disappearance of features along the depth. However, the system has the possibility to acquire images in smaller step sizes. The first image is taken from the top of the worm body. This panel shows the structure of the head and the mouth while the pharyngeal region is not visible. As the pharynx is structurally located in the middle sections, it becomes more visible as we scan closer to the mid-body and it then starts to fade away as the confocal imaging plane advances deeper. In the last slice, we are about to reach the other side of the body, and the entire pharyngeal region is slowly fading away. SECM images of Figure 4.9 demonstrate the slicing/confocal and depth-selective nature of developed SECM system.

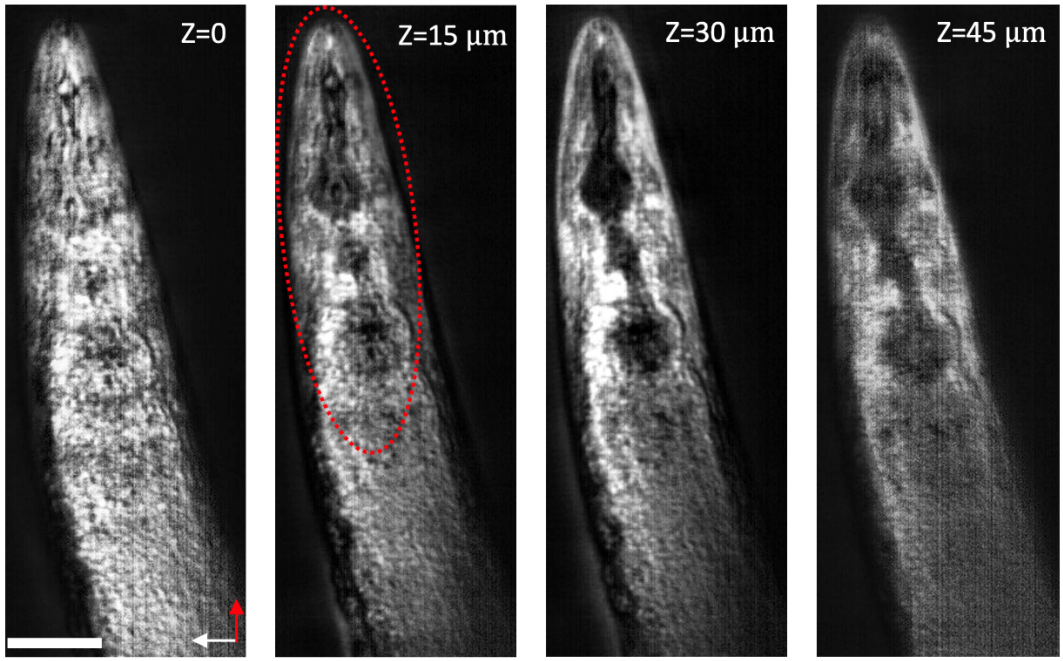

Fig. 4.9. Representative z-stack images of *C. elegans* pharyngeal region. Scale bar =50 µm. White and red arrows showing galvo scanning and spectrally encoded direction respectively.

One of the appealing characteristics of SECM is its high imaging speed which enables time-lapse confocal imaging of organs and/or body sections. Representative frames from the movement of head of a WT *C. elegans* are depicted in Figure 4.10. The SECM time-lapse

images can potentially be segmented and quantitatively analyzed to calculate the speed and frequency of *C. elegans* movement that is key for several categories of behavioral studies [62]. For example, correlation of maximum pharyngeal pumping rate with age in adult WT *C. elegans* [8], can be studied with our SECM system. Pharyngeal pumping is directly related to feeding regulation and often used as a phenotype for studying obesity and type 2 diabetes [59, 62]. Given the sharp contrast of the mouth, procorpus, metacorpus, isthmus, and posterior bulb, we anticipate SECM imaging to be specifically valuable for screening feeding disorders in *C. elegans.*

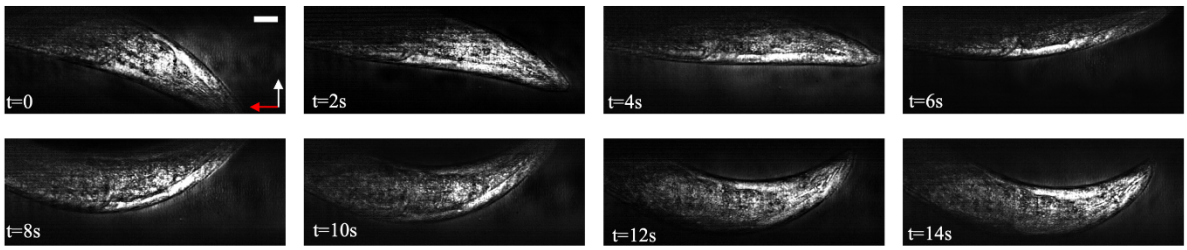

Fig. 4. 10. Representative frames from movement of at 2-second intervals. Scale bar =50 μm. White and red arrows showing galvo scanning and spectrally encoded direction respectively.

4.3. Mutant *C. elegans* imaging

Studying the genetic and phenotypic aspects of *C. elegans* mutant strains are commonplace in biology. In an abundant number of cases, mutations result in alterations of the physiology of targeted organs in *C. elegans,* most of which can be resolved by SECM and not necessarily by fluorescent imaging. Four mutant *C. elegans* with visible physiological irregularities have been chosen to study with SECM (Table 2).

Mutation in the MT2124 strain disrupts the intrinsic GTPase activity and causes protrusions on the worm body [11, 63]. These protrusions are called psuedovulvae since they are not functional [64]. The MT2124 strain is also a popular mutant associated with juvenile myelomonocytic

leukemia, cutaneous melanoma, and acute myeloid leukemia in humans [11]. Figure 4.11 presents SECM images of MT2124 worms with one psuedovulva (white arrowheads). Psuedovulva can clearly be recognized in the confocal image due to its different shape and appearance from that of a normal vulva (red arrowhead); accumulations of eggs in the body are also clearly resolved. SECM's ability in confocal resolution of vulva can be beneficial to *C. elegans* chemical screening and toxicity assays where the effective dose of chemicals on the shape, size, and formation of the vulva are investigated [11, 64].

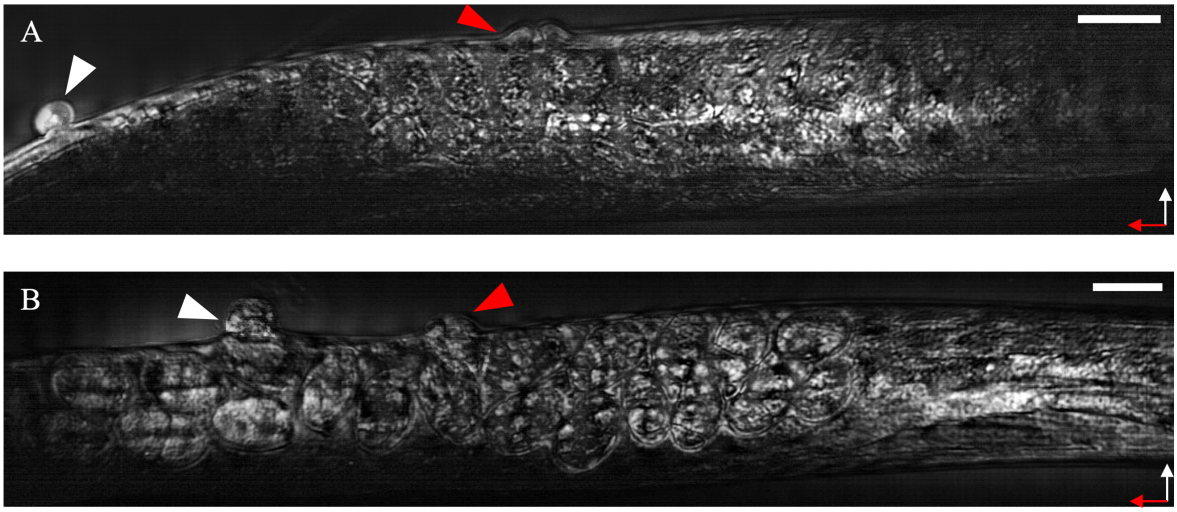

Fig. 4.11. The protrusions caused by the let-60 gene is visible (white arrowheads), and the difference between vulva (red arrowheads) and psuedovulva (white arrowheads) can be distinguished. Scale bar =50 μm. White and red arrows showing galvo scanning and spectrally encoded direction respectively.

The egl-1 gene is usually defined by GF (gain of function) mutations which can lead to the death of the hermaphrodite specific neurons (HSN). Since in *C. elegans* HSN is essential for egg-laying [65], the MT1082 strains are defective in reproduction and normally retain the late-stage eggs inside the body. A gravid *C. elegans* usually has ten to fifteen eggs in the uterus in adult stages. Figure 4.12(B) is a representative SECM image of a MT1082 worm. Accumulation of eggs inside the MT1082 adult *C. elegans* is clearly recognized when Figure 4.12 is compared

with image of a WT adult *C. elegans* presented in Figure 4.7. SECM's ability in high-speed confocal imaging of *C. elegans* eggs can enable automated quantification of egg size and quantity, which is critical for studies focusing on egl-1 regulation. In such studies, *C. elegans* egl-1 regulation is often correlated with the restriction of the BH3-only proteins in mammalians, which are activated by stress signals and are in the Bcl-2 family of proteins that control the mitochondrial pathway to apoptosis [66].

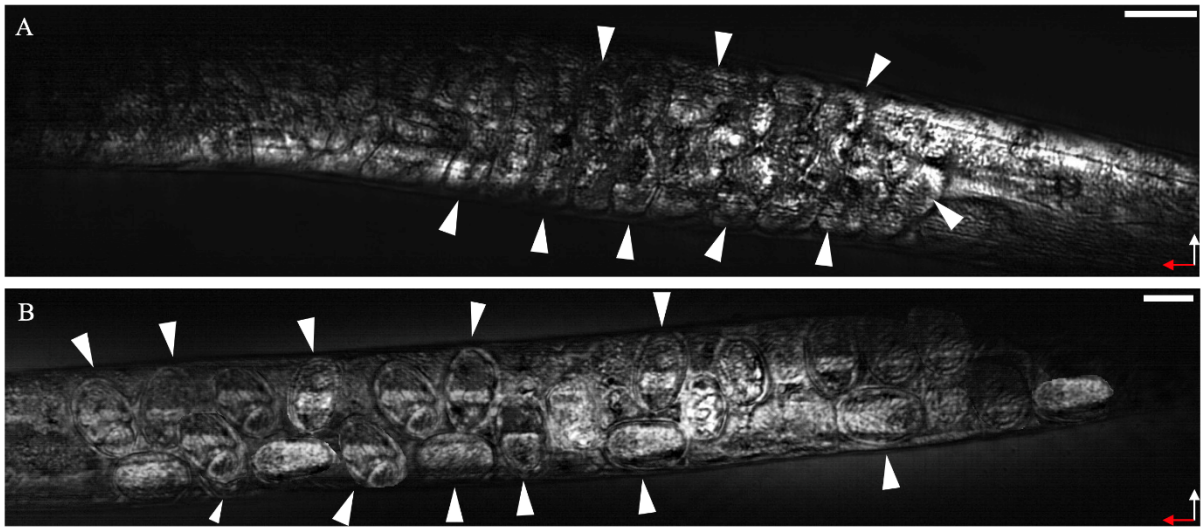

Fig. 4.12. A large number of eggs are visible in the middle body of the mutant worms are shown with white arrowheads. Scale bar =50 μm. White and red arrows showing galvo scanning and spectrally encoded direction respectively.

Reduction or loss of function in some cuticle collagen genes has resulted in a phenotype termed as dumpy (dpy), causing a significant decrease in worms' length, increased body diameter, and a delay in their growth and development [67]. For instance, the CB61 *C. elegans*, showing a loss of function in the dpy-5 gene (allele e-61), are used to investigate their dumpy phenotypes of smaller size and slow motion. The dpy-5 gene that makes the worms dumpy can cause diseases in humans such as osteogenesis imperfecta [68]. Figure 4.13 show representative images of a dumpy CB61 adult worms. Both worms have vulva and eggs, both of which are

indicators of the adult stage; nevertheless, the length of the worms are significantly shorter than that of WT *C. elegans* in the adult stage.

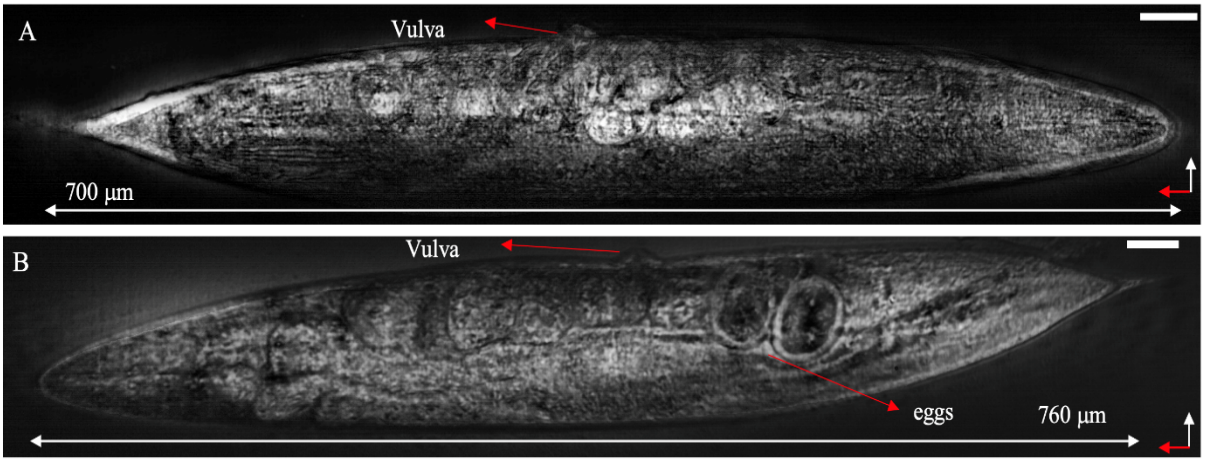

Fig. 4.13. Dumpy worms, the presence of vulva and eggs indicating worms are in the adult stage but shorter than an adult wild-type *C. elegans*. Scale bar =50 µm. White and red arrows showing galvo scanning and spectrally encoded direction respectively.

The gene e648 can cause defects in the head epidermal morphogenesis of *C. elegans* and eventually lead to the formation of a notched head [69]. That is, instead of an oval shape head, the CB648 strain exhibits irregularities on top of the head which can clearly be seen in the SECM image of Figure 4.14. The CB648 life cycle is longer than WT *C. elegans*, which takes them longer to reach the adult stage. SECM's ability to resolve the irregularities caused by e648 gene mutation is key for human disease models focusing on eye developmental defects such as aniridia and peters anomaly [69].

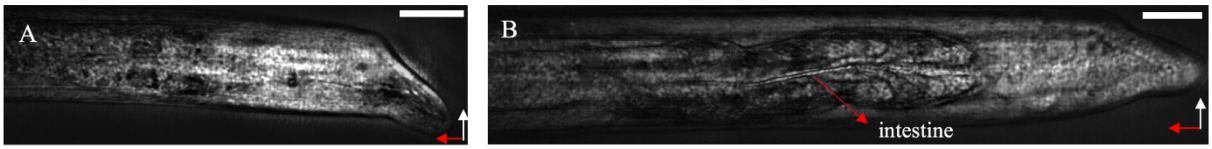

Fig. 4.14. head of the CB64 strain. Scale bar =50 µm. White and red arrows showing galvo scanning and spectrally encoded direction respectively.

Figures represented in this section demonstrate ability of SECM in resolving several mutation-induced structural hallmarks that are the target of numerous *C. elegans* studies.

4.4. Gold nano particles in *C. elegans*

Given the small size of *C. elegans*, microfluidic devices have been used as a platform for controlling the movement of *C. elegans* in high-throughput imaging and behavioural studies [70]. Given the satisfactory imaging performance of developed SECM system, we anticipate downstream integration of SECM in microfluidic platforms. To test feasibility, we used a T-shaped microfluidic device for loading the worms in the focal plane of the SECM system, immobilizing them, and finally imaging them. The worms used in this feasibility study were exposed to gold nano particles (GNPs). Research on effect of GNPs on *C. elegans* is quite popular due to GNPs abundancy in many man-made products and also in food and medical industries [71]. To study the interaction between nanoparticles and biological systems, the effect of nanoparticles on survival rate and reproductive performance of C. elegance can be investigated [71, 72]. To examine the capability of the system in detecting the presence of gold nanoparticles, GNPs with mean size of 10 nm (Sigma Aldrich, USA) were used in solutions with 100 mg/L and 200 mg/L concentrations. First, a high concentration of the gold nanoparticles solution (200 mg/L) was introduced into the channel. SECM was able to resolve the movement of the particles inside the channel due to the highly reflective nature of GNPs (Figure 4.15). Real-time images form the control and *C. elegans* exposed to 200 mg/L solution of GNP were also obtained by 20X objective. Representative frames are shown in Figure 4.16. Since the channel was already contaminated with GNP, in the control images the reflective pixels can be seen in panel A. The real-time images taken from the *C. elegans* exposed to GNP, however, show shiny particles inside the worm that synchronously move with the worm (green

arrows) and some are fixed shiny particles (blue arrows) in the channel. We assume the moving particles are the ones inside the worm body, and the stationary ones are in the channel and outside the nematode.

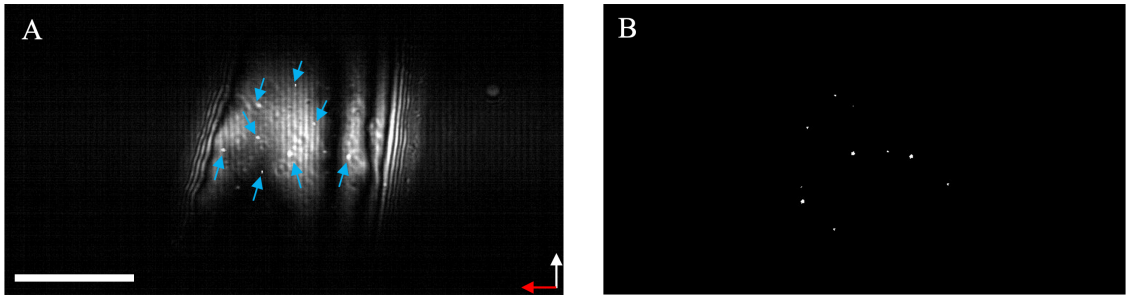

Fig. 4.15. A) SECM image showing a microfluidic channel containing GNPs (blue arrows). Scale bar = 50 µm. B) segmented particles in the channel.

To further investigate the presence of the GNP in *C. elegans*, SECM images were acquired from three group of control, exposed to 100 mg/L and 200 mg/L of worms. Unfortunately, the tests were not repeatable. We can think of two reasons to explain this failure. First, we need a reliable technique for introducing GNPs to worms. For example, microbial assays [72], can be used to ensure take up of GNPs by worms. Based on the literature [72, 73], exposure to GNPs affect the egg laying behaviours of worms; since, we did not see such correlation in our limited imaging sessions, we speculate that perhaps worms did not effectively consume the GNPs introduced to their environment. Second, the chosen nanoparticle are not very efficient reflectors of the 1310 nm wavelength. Utilization of gold nano rods in such studies are expected to enhance to reliability and repeatability of SECM imaging of GNPs.

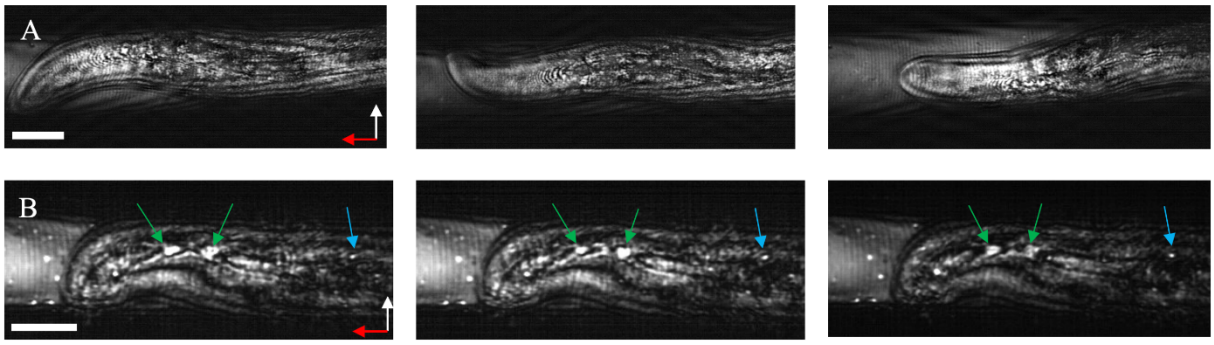

Fig. 4.16. (A) Control *C. elegans*, (B) *C. elegans* exposed to GNP. Green arrow showing the particles inside the worm which are moving with the worm movement, blue arrows showing fixed particles inside the channel and not the worm. Scale bar = 50 µm. White and red arrows showing galvo scanning and spectrally encoded direction respectively.

Chapter 5

Conclusion and future direction

This chapter provides the conclusion obtained in this research project. Potential future works in this area are also discussed.

5.1. Conclusion

A near infrared SECM system with an imaging line rate of up to 147 kHz has been developed to examine the feasibility of label-free high-speed confocal imaging of *C. elegans*. To the best of our knowledge this study is the first to report on high-speed label-free confocal microscopy of *C. elegans* with near infrared spectrally encoded confocal microscopy.

Modeling of the SECM system suggest a promising resolution and FOV to image model organisms. After developing the system, characterization tests indicated the developed system offers lateral and axial resolutions of ~2 μm and 10 μm with a 20X objective lens. The PSF and line distortion of the system was also evaluated and experimentally optimized through better alignment of optical components. A 50X objective lens was also used which offered improved

resolution, albeit with smaller FOV. SECM images of WT and mutant *C. elegans* and worms exposed to gold nanoparticles are presented and discussed. These results suggest that the developed system offers the resolution and contrast needed for visualization of key internal organs such as the pharyngeal region (mouth, isthmus, posterior bulb, and terminal bulb), vulva, egg, hatched larvae and lumen of the intestine. Mutation-induced structural hallmarks of MT2124, MT1082, CB61, and CB648 strains were also clearly resolved. This feasibility study demonstrates the promise of SECM for high-speed confocal imaging of *C. elegans* and is expected to open the door for downstream integration of SECM into microfluidic platforms to enable high-throughput physiological and behavioral phenotype screening of *C. elegans* populations. Despite the success of SECM in revealing organs in cellar resolution and physiological changes caused by mutations, there were issues associated with investigating the presence of gold nanoparticles in *C. elegans*.

5.2. Limitations and future direction

As a variant of reflectance confocal microscopy, the source of contrast in SECM is the scattering/reflection of light. To that end, SECM images provide information only on geometry and internal tissue structures of *C. elegans* and do not offer any insight into chemistry or molecular make up of tissue. Chemical specificity can potentially be achieved in SECM by administration of antibody-conjugated contrast agents targeting the molecule(s) of interest.

The SECM system used in this study incorporated a light source with center wavelength of 1.3μm. While smaller center wavelengths (e.g., 800nm) offer better imaging resolution, we believe that the 1.3μm center wavelength is a better fit for SECM imaging in microfluidic platforms because these devices are normally based on poly-dimethylsiloxane (PDMS) which exhibits its visible-NIR minimal light absorption at 1320nm [74].

One of the challenges of SECM imaging of *C. elegans* is reliable and repeatable positioning of the nematode in the field of view of the system. To overcome this issue, we are currently developing microfluidic platforms for automated loading and unloading of the worms in the system.

Given the ~60 μm diameter of *C. elegans*, improvement of the axial resolution of system is another consideration for our future work. We aim to use tapered fibers with smaller core diameters (i.e., the confocal microscope's pinhole) to improve the axial resolution of the system.

To improve the spectral resolution of SECM a telescopic beam expander with a different magnification can be used in imaging arm before the diffraction grating. In this way the diameter of the beam over the grating will increase which consequently improves the resolving power of the grating.

Due to widespread use of nanoparticles (NPs) in pharmaceutical and food industry it would be interesting to study the effect of nanoparticles on *C. elegans*. Previously we investigated the effect of GNPs in *C. elegans*, however other NPs such gold nano rods or carbon nanomaterials can also cause endocytosis in *C. elegans* [72]. Moreover, gold nano rods or carbon nanomaterials have a higher scattering in the wavelength spectrum implemented in developed SECM system.

Once these improvements are achieved, we intend to examine the possibility of performing high-throughput imaging of worm populations in microfluidic platforms (as shown in spectrally encoded flow cytometry [75]). Figure 5.1 depicts the conceptual design of such system where worm cross sections are continuously imaged as population of worms are passed though the microchannel. The movement of worms should be controlled in order to have a constant movement speed in the imaging area. Post-processing of acquired images can potentially enable

3D reconstruction of worm geometry and structures. Given the 147 kHz line rate of developed system the 60μm-diameter of the microchannel can be imaged with a 0.4 μm spatial sampling period at a temporal rate of 980 frames per second. Such high imaging speed can theoretically accommodate 3D confocal imaging of *C. elegans* at an unprecedented speed of ~10 worms per second with voxel size of 0.4×0.4×10 μm^3.

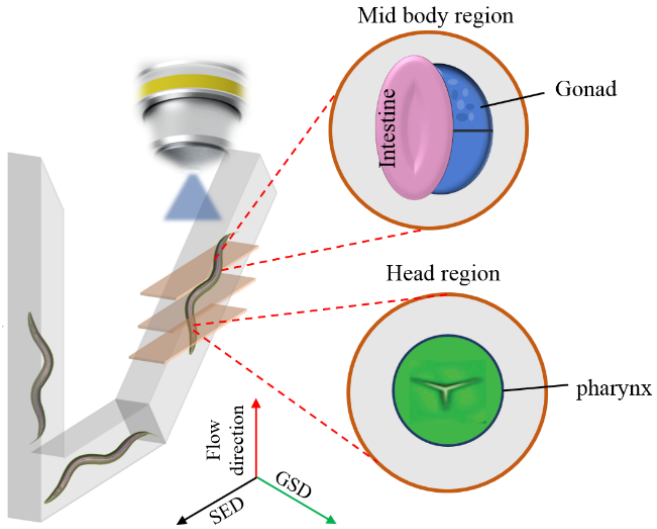

Fig. 5.1. Conceptual design of SECM system for high-throughput 3D imaging of *C. elegans*. GSD: Galvo scanning direction, SED: Spectrally encoded direction.

References

1. S. Leonelli and R. A. Ankeny, "What makes a model organism?," Endeavour **37**, 209-212 (2013).
2. A. G. Little, M. E. Pamenter, D. Sitaraman, N. M. Templeman, W. G. Willmore, M. S. Hedrick, and C. D. Moyes, "Utilizing comparative models in biomedical research," Comparative Biochemistry and Physiology Part A: Molecular & Integrative Physiology **256**, 110938 (2021).
3. C. K. Leung, Y. Wang, S. Malany, A. Deonarine, K. Nguyen, S. Vasile, and K. P. Choe, "An ultra high-throughput, whole-animal screen for small molecule modulators of a specific genetic pathway in Caenorhabditis elegans," PloS one **8**, e62166 (2013).
4. M. Markaki and N. Tavernarakis, "Modeling human diseases in Caenorhabditis elegans," Biotechnology journal **5**, 1261-1276 (2010).
5. H. E. Kinser and Z. Pincus, "High-throughput screening in the C. elegans nervous system," Molecular and Cellular Neuroscience **80**, 192-197 (2017).
6. E. Teshiba, K. Miyahara, and H. Takeya, "Glucose-induced abnormal egg-laying rate in Caenorhabditis elegans," Bioscience, Biotechnology, and Biochemistry **80**, 1436-1439 (2016).
7. J. Apfeld and S. Alper, "What Can We Learn About Human Disease from the Nematode C. elegans?," Methods Mol Biol **1706**, 53-75 (2018).
8. M. J. Rodríguez-Palero, A. López-Díaz, R. Marsac, J.-E. Gomes, M. Olmedo, and M. Artal-Sanz, "An automated method for the analysis of food intake behaviour in Caenorhabditis elegans," Scientific reports **8**, 1-10 (2018).
9. Z. F. a. H. Altun, D.H, "Introductio," in *WormAtlas,* L. A. Herndon, ed. (WormAtlas, 2009).
10. J. F. Cooper and J. M. Van Raamsdonk, "Modeling Parkinson's Disease in C. elegans," Journal of Parkinson's disease **8**, 17-32 (2018).
11. P. M. Medina, J. M. Ponce, and C. A. Cruz, "Revealing the anticancer potential of candidate drugs in vivo using Caenorhabditis elegans mutant strains," Translational oncology **14**, 100940 (2021).
12. K. Youssef, A. Tandon, and P. Rezai, "Studying Parkinson's disease using Caenorhabditis elegans models in microfluidic devices," Integrative Biology **11**, 186-207 (2019).
13. A. Nwaneshiudu, C. Kuschal, F. H. Sakamoto, R. R. Anderson, K. Schwarzenberger, and R. C. Young, "Introduction to confocal microscopy," Journal of Investigative Dermatology **132**, 1-5 (2012).
14. D. Semwogerere and E. R. Weeks, "Confocal microscopy," Encyclopedia of biomaterials and biomedical engineering **23**, 1-10 (2005).
15. A. R. Hardham, "Confocal microscopy in plant–pathogen interactions," in *Plant Fungal Pathogens* (Springer, 2012), pp. 295-309.
16. A. S. Maddox and P. S. Maddox, "High-resolution imaging of cellular processes in Caenorhabditis elegans," Methods in cell biology **107**, 1-34 (2012).
17. C. Martin, T. Li, E. Hegarty, P. Zhao, S. Mondal, and A. Ben-Yakar, "Line excitation array detection fluorescence microscopy at 0.8 million frames per second," Nature Communications **9**, 4499 (2018).
18. J. Van Krugten, K. K. H. Taris, and E. J. G. Peterman, "Imaging adult C. elegans live using light-sheet microscopy," Journal of Microscopy **281**, 214-223 (2021).
19. T.-Y. Hsieh, S. Vyas, J.-C. Wu, and Y. Luo, "Volume holographic optical element for light sheet fluorescence microscopy," Optics Letters **45**, 6478-6481 (2020).

20. E. J. Gualda, H. Pereira, G. G. Martins, R. Gardner, and N. Moreno, "Three-dimensional imaging flow cytometry through light-sheet fluorescence microscopy," Cytometry Part A **91**, 144-151 (2017).
21. M. Rubart, "Two-photon microscopy of cells and tissue," Circulation research **95**, 1154-1166 (2004).
22. G. Filippidis, C. Kouloumentas, G. Voglis, F. Zacharopoulou, T. G. Papazoglou, and N. Tavernarakis, "Imaging of Caenorhabditis elegans neurons by second-harmonic generation and two-photon excitation fluorescence," Journal of biomedical optics **10**, 024015 (2005).
23. S. Coquoz, P. J. Marchand, A. Bouwens, L. Mouchiroud, V. Sorrentino, D. Szlag, J. Auwerx, and T. Lasser, "Label-free three-dimensional imaging of Caenorhabditis elegans with visible optical coherence microscopy," PloS one **12**, e0181676 (2017).
24. L. Breimann, F. Preusser, and S. Preibisch, "Light-microscopy methods in C. elegans research," Current Opinion in Systems Biology **13**, 82-92 (2019).
25. J. Martel, C. Y. Wu, H. H. Peng, Y. F. Ko, H. C. Yang, J. D. Young, and D. M. Ojcius, "Plant and fungal products that extend lifespan in Caenorhabditis elegans," Microbial cell (Graz, Austria) **7**, 255-269 (2020).
26. J. Oh, S. H. Kim, Y. J. Kim, H. Lee, J. H. Cho, Y. H. Cho, C.-K. Kim, T. J. Lee, S. Lee, and K. H. Park, "Detection of retinitis pigmentosa by differential interference contrast microscopy," PloS one **9**, e97170 (2014).
27. Z. F. a. H. Altun, D.H, "Nervous system, general description," in *WormAtlas,* L. A. Herndon, ed. (WormAtlas, 2013).
28. A. Agrawal, T. J. Pfefer, P. D. Woolliams, P. H. Tomlins, and G. Nehmetallah, "Methods to assess sensitivity of optical coherence tomography systems," Biomedical optics express **8**, 902-917 (2017).
29. H. L. Bartlett, R. B. Escalera, 2nd, S. S. Patel, E. W. Wedemeyer, K. A. Volk, J. L. Lohr, and B. E. Reinking, "Echocardiographic assessment of cardiac morphology and function in Xenopus," Comparative medicine **60**, 107-113 (2010).
30. G. J. Tearney, R. H. Webb, and B. E. Bouma, "Spectrally encoded confocal microscopy," Optics letters **23**, 1152-1154 (1998).
31. C. Boudoux, "Wavelength swept spectrally encoded confocal microscopy for biological and clinical applications," Massachusetts Institute of Technology, 2007).
32. C. Boudoux, S. H. Yun, W.-Y. Oh, W. M. White, N. V. Iftimia, M. Shishkov, B. E. Bouma, and G. J. Tearney, "Rapid wavelength-swept spectrally encoded confocal microscopy," Optics Express **13**, 8214-8221 (2005).
33. J. Hwang, S. Kim, J. Heo, D. Lee, S. Ryu, and C. Joo, "Frequency-and spectrally-encoded confocal microscopy," Optics express **23**, 5809-5821 (2015).
34. D. Kang, M. J. Suter, C. Boudoux, H. Yoo, P. S. Yachimski, W. P. Puricelli, N. S. Nishioka, M. Mino-Kenudson, G. Y. Lauwers, and B. E. Bouma, "Comprehensive imaging of gastroesophageal biopsy samples by spectrally encoded confocal microscopy," Gastrointestinal endoscopy **71**, 35-43 (2010).
35. L. Golan and D. Yelin, "Flow cytometry using spectrally encoded confocal microscopy," Opt Lett **35**, 2218-2220 (2010).
36. L. Golan, D. Yeheskely-Hayon, L. Minai, E. J. Dann, and D. Yelin, "Noninvasive imaging of flowing blood cells using label-free spectrally encoded flow cytometry," Biomed Opt Express **3**, 1455-1464 (2012).
37. L. Golan and D. Yelin, "Flow cytometry using spectrally encoded confocal microscopy," Optics letters **35**, 2218-2220 (2010).

38. H. Yoo, D. Kang, A. J. Katz, G. Y. Lauwers, N. S. Nishioka, Y. Yagi, P. Tanpowpong, J. Namati, B. E. Bouma, and G. J. Tearney, "Reflectance confocal microscopy for the diagnosis of eosinophilic esophagitis: a pilot study conducted on biopsy specimens," Gastrointestinal endoscopy **74**, 992-1000 (2011).
39. S. C. Schlachter, D. Kang, M. J. Gora, P. Vacas-Jacques, T. Wu, R. W. Carruth, E. J. Wilsterman, B. E. Bouma, K. Woods, and G. J. Tearney, "Spectrally encoded confocal microscopy of esophageal tissues at 100 kHz line rate," Biomedical optics express **4**, 1636-1645 (2013).
40. D. Kang, H. Yoo, P. Jillella, B. E. Bouma, and G. J. Tearney, "Comprehensive volumetric confocal microscopy with adaptive focusing," Biomedical optics express **2**, 1412-1422 (2011).
41. N. Tabatabaei, D. Kang, T. Wu, M. Kim, R. W. Carruth, J. Leung, J. S. Sauk, W. Shreffler, Q. Yuan, and A. Katz, "Tethered confocal endomicroscopy capsule for diagnosis and monitoring of eosinophilic esophagitis," Biomedical optics express **5**, 197-207 (2014).
42. D. Kang, R. W. Carruth, M. Kim, S. C. Schlachter, M. Shishkov, K. Woods, N. Tabatabaei, T. Wu, and G. J. Tearney, "Endoscopic probe optics for spectrally encoded confocal microscopy," Biomed Opt Express **4**, 1925-1936 (2013).
43. N. Tabatabaei, D. Kang, M. Kim, T. Wu, C. N. Grant, M. Rosenberg, N. S. Nishioka, P. E. Hesterberg, J. Garber, and Q. Yuan, "Clinical translation of tethered confocal microscopy capsule for unsedated diagnosis of eosinophilic esophagitis," Scientific reports **8**, 1-9 (2018).
44. J. Kim, D. Kang, and D. Gweon, "Spectrally encoded slit confocal microscopy," Optics letters **31**, 1687-1689 (2006).
45. K. Soocheol, H. Jaehyun, H. Jung, R. Su-Ho, L. Donghak, K. Sang-Hoon, O. Seung Jae, and J. Chulmin, "Spectrally encoded slit confocal microscopy using a wavelength-swept laser," Journal of biomedical optics **20**, 1-5 (2015).
46. E. E. Freeman, A. Semeere, H. Osman, G. Peterson, M. Rajadhyaksha, S. González, J. N. Martin, R. R. Anderson, G. J. Tearney, and D. Kang, "Smartphone confocal microscopy for imaging cellular structures in human skin in vivo," Biomedical optics express **9**, 1906-1915 (2018).
47. C. Gong, D. B. Stratton, C. N. Curiel-Lewandrowski, and D. Kang, "Speckle-free, near-infrared portable confocal microscope," Applied optics **59**, G41-G46 (2020).
48. C. Gong, N. Kulkarni, W. Zhu, C. D. Nguyen, C. Curiel-Lewandrowski, and D. Kang, "Low-cost, high-speed near infrared reflectance confocal microscope," Biomedical optics express **10**, 3497-3505 (2019).
49. D. Yelin, B. E. Bouma, S. H. Yun, and G. J. Tearney, "Double-clad fiber for endoscopy," Optics letters **29**, 2408-2410 (2004).
50. T. Stiernagle, "Maintenance of C. elegans," in *Wormbook,* T. C. e. r. community, ed. (Wormbook, 2006).
51. M. Porta-de-la-Riva, L. Fontrodona, A. Villanueva, and J. Cerón, "Basic Caenorhabditis elegans methods: synchronization and observation," Journal of visualized experiments : JoVE, e4019 (2012).
52. S. Shaham, "WormBook: Methods in Cell Biology," in *Wormbook,* T. C. e. r. community, ed. (Wormbook, 2006).
53. W. R. Schafer, "Genetics of Egg-Laying in Worms," Annual Review of Genetics **40**, 487-509 (2006).
54. L. McMahon, J. M. Muriel, B. Roberts, M. Quinn, and I. L. Johnstone, "Two sets of interacting collagens form functionally distinct substructures within a Caenorhabditis elegans extracellular matrix," Molecular biology of the cell **14**, 1366-1378 (2003).
55. A. D. Chisholm and H. R. Horvitz, "Patterning of the Caenorhabditis elegans head region by the Pax-6 family member vab-3," Nature **377**, 52-55 (1995).

56. A. J. Nichols and C. L. Evans, "Video-rate scanning confocal microscopy and microendoscopy," Journal of visualized experiments : JoVE (2011).
57. O. Haeberlé, M. Ammar, H. Furukawa, K. Tenjimbayashi, and P. Török, "Point spread function of optical microscopes imaging through stratified media," Optics Express **11**, 2964-2969 (2003).
58. A. Schlotterer, G. Kukudov, F. Bozorgmehr, H. Hutter, X. Du, D. Oikonomou, Y. Ibrahim, F. Pfisterer, N. Rabbani, and P. Thornalley, "C. elegans as model for the study of high glucose–mediated life span reduction," Diabetes **58**, 2450-2456 (2009).
59. S. Hashmi, Y. Wang, R. S. Parhar, K. S. Collison, W. Conca, F. Al-Mohanna, and R. Gaugler, "A C. elegans model to study human metabolic regulation," Nutr Metab (Lond) **10**, 31-31 (2013).
60. E. Kyriakakis, M. Markaki, and N. Tavernarakis, "Caenorhabditis elegans as a model for cancer research," Molecular & cellular oncology **2**, e975027 (2015).
61. M. Gardner, M. Rosell, and E. M. Myers, "Measuring the effects of bacteria on C. elegans behavior using an egg retention assay," Journal of visualized experiments : JoVE, e51203 (2013).
62. K. T. Jones and K. Ashrafi, "Caenorhabditis elegans as an emerging model for studying the basic biology of obesity," Disease models & mechanisms **2**, 224-229 (2009).
63. F. Chen, A. D. Mackerell, Jr., Y. Luo, and P. Shapiro, "Using Caenorhabditis elegans as a model organism for evaluating extracellular signal-regulated kinase docking domain inhibitors," J Cell Commun Signal **2**, 81-92 (2008).
64. D. J. Reiner, V. González-Pérez, C. J. Der, and A. D. Cox, "Use of Caenorhabditis elegans to evaluate inhibitors of Ras function in vivo," Methods in enzymology **439**, 425-449 (2008).
65. B. Conradt and H. R. Horvitz, "The C. elegans protein EGL-1 is required for programmed cell death and interacts with the Bcl-2-like protein CED-9," Cell **93**, 519-529 (1998).
66. R. Nehme and B. Conradt, "egl-1: a key activator of apoptotic cell death in C. elegans," Oncogene **27**, S30-S40 (2008).
67. C. Thacker, J. A. Sheps, and A. M. Rose, "Caenorhabditis elegans dpy-5 is a cuticle procollagen processed by a proprotein convertase," Cellular and Molecular Life Sciences CMLS **63**, 1193-1204 (2006).
68. M. Watanabe, N. Mitani, N. Ishii, and K. Miki, "A mutation in a cuticle collagen causes hypersensitivity to the endocrine disrupting chemical, bisphenol A, in Caenorhabditis elegans," Mutation Research/Fundamental and Molecular Mechanisms of Mutagenesis **570**, 71-80 (2005).
69. H. N. Cinar and A. D. Chisholm, "Genetic analysis of the Caenorhabditis elegans pax-6 locus: roles of paired domain-containing and nonpaired domain-containing isoforms," Genetics **168**, 1307-1322 (2004).
70. S. Saberi-Bosari, J. Huayta, and A. San-Miguel, "A microfluidic platform for lifelong high-resolution and high throughput imaging of subtle aging phenotypes in C. elegans," Lab on a chip **18**, 3090-3100 (2018).
71. L. Gonzalez-Moragas, P. Berto, C. Vilches, R. Quidant, A. Kolovou, R. Santarella-Mellwig, Y. Schwab, S. Stürzenbaum, A. Roig, and A. Laromaine, "In vivo testing of gold nanoparticles using the Caenorhabditis elegans model organism," Acta biomaterialia **53**, 598-609 (2017).
72. J. Moon, J. I. Kwak, S. W. Kim, and Y.-J. An, "Multigenerational effects of gold nanoparticles in Caenorhabditis elegans: Continuous versus intermittent exposures," Environmental pollution **220**, 46-52 (2017).
73. S. W. Kim, J. I. Kwak, and Y.-J. An, "Multigenerational study of gold nanoparticles in Caenorhabditis elegans: transgenerational effect of maternal exposure," Environmental science & technology **47**, 5393-5399 (2013).

74. C. Markos, K. Vlachos, and G. Kakarantzas, "Guiding and thermal properties of a hybrid polymer-infused photonic crystal fiber," Optical Materials Express **2**, 929-941 (2012).
75. A. Zeidan, L. Golan, and D. Yelin, "In vitro hematocrit measurement using spectrally encoded flow cytometry," Biomedical optics express **7**, 4327-4334 (2016).